Impacts of Global Open Fire Aerosols on Direct Radiative, Cloud and Surface-Albedo Effects Simulated with CAM5

Yiquan Jiang[1,2], Zheng Lu[2], Xiaohong Liu[2,*], Yun Qian[3], Kai Zhang[3], Yuhang Wang[4] and Xiu-Qun Yang[1]

[1] *CMA-NJU Joint Laboratory for Climate Prediction Studies, Institute for Climate and Global Change Research, School of Atmospheric Sciences, Nanjing University, Nanjing, China*

[2] *Department of Atmospheric Science, University of Wyoming*

[3] *Pacific Northwest National Laboratory, Richland, Washington, USA*

[4] *School of Earth and Atmospheric Sciences, Georgia Institute of Technology, Atlanta, Georgia, USA*

*Corresponding author:

Dr. Xiaohong Liu
Department of Atmospheric Science
University of Wyoming
Laramie, WY 82071
Phone (307) 766-3225
E-mail: xliu6@uwyo.edu

Abstract

Aerosols from open-land fires could significantly perturb the global radiation balance and induce the climate change. In this study, Community Atmospheric Model version 5 (CAM5) with prescribed daily fire aerosol emissions is used to investigate the spatial and seasonal characteristics of radiative effects (REs, relative to the case of no fires) of open fire aerosols including black carbon (BC) and particulate organic matter (POM) from 2003 to 2011. The global annual mean RE due to aerosol-radiation interactions (REari) of all fire aerosols is 0.16±0.01 W m^{-2} (1σ uncertainty), mainly due to the absorption of fire BC (0.25±0.01 W m^{-2}), while fire POM induces a small overall effect (-0.05 W m^{-2} and 0.04±0.01 W m^{-2}, respectively based on two methods). Strong positive REari is found in the Arctic and in the oceanic regions west of southern Africa and South America as a result of amplified absorption of fire BC above low-level clouds, in general agreement with satellite observations. The global annual mean RE due to aerosol-cloud interactions (REaci) of all fire aerosols is -0.70±0.05 W m^{-2}, resulting mainly from the fire POM effect (-0.59±0.03 W m^{-2}). REari (0.43±0.03 W m^{-2}) and REaci (-1.38±0.23 W m^{-2}) in the Arctic are stronger than those in the tropics (0.17±0.02 and -0.82±0.09 W m^{-2}, respectively for REari and REaci), although the fire aerosol burden is higher in the tropics. The large cloud liquid water path over land areas and low solar zenith angle of the Arctic favor the strong fire aerosol REaci (up to -15 W m^{-2}) during the Arctic summer. Significant surface cooling, precipitation reduction and low-level cloud amount increase are also found in the Arctic summer as a result of the fire aerosol REaci based on the atmosphere-only simulations. The global annual mean RE due to

surface albedo changes (REsac) over land areas (0.03 ± 0.10 W m^{-2}) is small and statistically insignificant, and is mainly due to the fire BC-in-snow effect (0.02 W m^{-2}) with the maximum albedo effect occurring in spring (0.12 W m^{-2}) when snow starts to melt.

1. Introduction

Open fires or biomass burning of living and dead vegetation are an integral component of the Earth system, and have significant impacts on the carbon cycle [*Ciais et al.*, 2013] and the climate [*Bowman et al.*, 2009; *Keywood et al.*, 2011; *Liu et al.*, 2014; *Sommers et al.*, 2014; *Voulgarakis and Field*, 2015]. On one hand, open fires can perturb the climate system by emitting greenhouse gases and aerosols [*Kaiser et al.*, 2012; *Wiedinmyer et al.*, 2011]. On the other hand, climate states and variabilities can play a critical role in determining the occurrence frequency and intensity of open fires [*Marlon et al.*, 2009; *van der Werf et al.*, 2008; *Westerling et al.*, 2006; *Bistinas et al.*, 2014]. However, there are still large unknowns regarding the feedback mechanisms between open fire and climate interactions [*Carslaw et al.*, 2010; *Liu et al.*, 2014]. A qualification of radiative forcing of fire aerosols as conducted in this study is the first step to reduce these uncertainties.

Particles emitted from open fires can exert significant perturbations to the climate system by scattering and absorbing the solar radiation in the atmosphere (i.e., direct effect) [*Carslaw et al.*, 2010] and by changing the surface albedo when they are deposited on the snow and ice (i.e., surface albedo effect) [*Flanner et al.*, 2007; *Quinn et al.*, 2008; *Randerson et al.*, 2006; *Qian et al.*, 2011, 2015]. In addition, open fire or

76 smoke particles can modify the cloud properties, precipitation efficiency, and the
77 hydrological cycle by changing the atmospheric thermal structure (i.e., semi-direct
78 effect) [*Koch and Del Genio*, 2010; *Andreae et al.*, 2004b] or acting as cloud
79 condensation nuclei (CCN) (i.e., indirect effects) [*Andreae and Rosenfeld*, 2008; *Qian*
80 *et al.*, 2009; *Lu and Sokolik*, 2013].

81 The radiative effect (RE) [*Boucher and Tanre*, 2000] and radiative forcing (RF)
82 [*Forster et al.*, 2007; *Myhre et al.*, 2013a] are typical metrics used to assess and
83 compare anthropogenic and natural drivers of climate change. The aerosol RE
84 represents the instantaneous radiative impact of atmospheric particles on the Earth's
85 energy balance [*Heald et al.*, 2014]. RF is calculated as the change of RE between
86 two different periods, e.g., the pre-industrial and the present-day times [*Heald et al.*,
87 2014; *Liu et al.*, 2007], based on the aerosol and precursor gas emissions in the two
88 periods [*Dentener et al.*, 2006; *Lamarque et al.*, 2010].

89 RF due to aerosol and radiation interactions (RFari) of biomass burning aerosols
90 has been estimated since the IPCC second Assessment Report (AR2). Based on the
91 Aerosol Comparisons between Observations and Models (AeroCom) Phase II
92 simulations [*Bond et al.*, 2013; *Myhre et al.*, 2013b], RFari of biomass burning
93 aerosols in the IPCC Fifth Assessment Report (AR5) is estimated to be 0.0 W m^2
94 (ranging from -0.20 to 0.20 W m^{-2}), and RFari of biomass burning black carbon (BC)
95 and primary organic matter (POM) are of the opposite sign (i.e., 0.10 and -0.10 W m^{-2},
96 respectively).

97 There are also some studies that estimated the RE due to aerosol and radiation

98 interactions (REari) of fire aerosols by comparing the simulation with fire emissions
99 against the simulation with no fire emissions. For example, using the NCAR
100 Community Atmosphere Model version 4 (CAM4) with a bulk aerosol module, *Tosca*
101 *et al.* [2013] reported that the top-of-atmosphere (TOA) REari from global biomass
102 burning aerosols is 0.18±0.10 W m^{-2} averaged for the period of 1997-2009. *Ward et al.*
103 [2012] estimated the REari from biomass burning aerosols in the pre-industrial (for
104 the year 1850), present-day (for the year 2000), and future time periods (for the year
105 2100), and found that the biomass burning aerosol REari for the year 2000 is 0.13 W
106 m^{-2} and -0.27 W m^{-2} in all-sky and clear-sky conditions, respectively.
107 RE due to aerosol and cloud interactions (REaci) of biomass burning aerosols can
108 be comparable in magnitude to or even stronger than the REari [*Liu et al.*, 2014].
109 With a global aerosol-climate model, the REaci of biomass burning aerosols was
110 estimated to range from -1.74 to -1.00 W m^{-2} for the year 2000 in *Ward et al.* [2012].
111 The semi-direct radiative effect of biomass burning aerosols is not independently
112 assessed in IPCC reports. The magnitude was reported to be about 7.0 W m^{-2} in the
113 Southern American biomass burning regions by examining the radiative flux
114 difference with and without the biomass burning aerosol effect on clouds [*Liu*, 2005].
115 The RF or RE due to surface albedo changes (RFsac or REsac) of BC from open
116 fires and other sources has been estimated in previous studies. For biomass burning
117 emissions with a strong (1998) and weak (2001) boreal fire year, RE of fire
118 BC-in-snow was estimated to be 0.011 and 0.006 W m^{-2}, respectively [*Flanner et al.*,
119 2007]. *Randerson et al.* [2006] reported that BC from a boreal forest fire deposited on

120 snow and sea ice introduced a global annual mean RE of 8±5 W per m^2 of burned area
121 in the first year when the fire happened. A summary of BC-in-snow forcing/effect can
122 be found in *Bond et al*. [2013]. They reported that the present-day RE of fire
123 BC-in-snow ranges from 0.006 to 0.02 W m^{-2} based on previous studies [*Jacobson*,
124 2004; *Rypdal et al.*, 2009; *Skeie et al.*, 2011; *Hansen et al.*, 2005; *Flanner et al.*, 2007,
125 2009; *Koch et al.*, 2009].

126 Biomass burning aerosols can have significant impacts on global and regional
127 precipitation and atmospheric circulation. With the change of fire emissions from year
128 1860 to 2000, *Jones et al.* [2007] found that biomass burning aerosols decrease the
129 global near-surface air temperature by about 0.25°C, when considering the feedbacks
130 of sea surface temperature (SST) in the model. As shown in *Tosca et al.* [2013], the
131 direct and semi-direct effects of biomass burning aerosols reduce the precipitation
132 near the equator and weaken the Hadley circulation. With a regional climate model,
133 *Zhang et al.* [2009] found that biomass burning aerosols may warm and stabilize the
134 lower troposphere and thus reinforce the dry season rainfall pattern in the Southern
135 Amazonia. The absorption of shortwave radiation by biomass burning BC could
136 increase the vertical stratification and inhibit both the cloud formation and
137 precipitation [*Ackerman et al.*, 2000; *Tosca et al.*, 2014]. In contrast, biomass burning
138 aerosols could invigorate the convective clouds [*Andreae et al.*, 2004a; *Koren et al.*,
139 2005] through suppressing warm rain processes in the convection, and enhance the
140 latent heat release at higher levels [*Andreae and Rosenfeld*, 2008].

141 Although there have been many studies quantifying the RE of fire aerosols, a

142 further investigation is still needed, as the current estimations of fire aerosol RE are
143 still associated with large uncertainties [e.g., *Myhre and Samset*, 2015; *Chakrabarty et*
144 *al.*, 2014]. The REs of co-emitted fire POM versus BC are even less clear. In this
145 study, we estimate the present day (from year 2003 to 2011) open fire aerosol REs
146 (including REari, REaci and REsac) using the NCAR Community Atmosphere Model
147 version 5.3 (CAM5) with the four-mode version of the modal aerosol module
148 (MAM4). We use two methods to calculate the REari of fire aerosols (total, BC-only,
149 and POM-only). One method estimates the REari based on different model
150 simulations [*Ghan*, 2013], and the other one calculates the REari directly through
151 multiple diagnostic radiation calls in a single simulation. The spatial and seasonal
152 characteristics of fire aerosol REs, and the impacts on the global precipitation and
153 temperature are discussed.

154 Compared to earlier studies of fire aerosol REs [*Tosca et al.*, 2013; *Ward et al.*,
155 2012], a number of improvements are made in this study. First, a higher model
156 horizontal resolution at 0.9° by 1.25° is used versus 1.9° by 2.5°. The higher
157 resolution allows more efficient transport of aerosols from the sources to remote
158 regions [*Ma et al*., 2013; 2014]. Model resolution has also been shown to be important
159 for aerosol REaci [*Ma et al*., 2015]. Second, the latest CAM5 model with MAM4 is
160 used. MAM4 with an additional primary carbon mode explicitly treats the
161 microphysical ageing of primary carbonaceous aerosols (POM/BC) in the atmosphere.
162 MAM4 has higher BC and POM burdens over the earlier three-mode version of
163 MAM (MAM3) in the remote regions by ~30% [*Liu et al.*, 2016]. Third, daily instead

of monthly fire emissions are used, which allows the model to consider the effect of fast changes in the fire emission flux on local atmospheric conditions. It is expected that using the monthly mean emission flux the model can not consider the effect of extremely strong fires, thus it might underestimate the fire aerosol REs for such cases. Finally, a new methodology [*Ghan*, 2013] is used to more accurately diagnose the REs of fire aerosols. Central to this method is that the REari must be calculated in the presence of clouds (i.e., under the all-sky condition), and the REaci be calculated under the condition of no aerosol effects on radiation. With the radiative forcing decomposition of this method, REsac can also be quantified.

The paper is organized as follows. Section 2 introduces the model and experiments. Section 3 describes the methods to diagnose the fire aerosol REs. Section 4 presents the model results of fire aerosol REs, and impacts on global and regional surface temperature and precipitation. Conclusions and discussion are given in Section 5.

2. Model, Experiment Design and Aerosol Radiative Effect Method

2.1 Model

In our study, we use the Community Earth System Model (CESM) version 1.2, with the Community Atmosphere Model version 5.3 (CAM5.3) [*Neale et al.*, 2010] coupled with the Community Land Model version 4 (CLM4) [*Oleson et al.*, 2010]. The SNow, ICe, and Aerosol Radiative model (SNICAR) [*Flanner and Zender*, 2005] is turned on in the simulations to diagnose the biomass burning BC-in-snow effect. CAM5 includes several major updates in its physics parameterizations compared to

187 previous CAM versions. A two-moment stratiform cloud microphysics scheme is
188 included in CAM5 to predict both the mass and number mixing ratios of cloud liquid
189 and cloud ice [*Morrison and Gettelman*, 2008]. MAM4, which was updated from
190 MAM3 [*Liu et al.*, 2012], includes aerosol mass and number mixing ratios in four
191 lognormal modes: Aitken, accumulation, coarse, and primary carbon mode [*Liu et al.*,
192 2016]. An additional primary carbon mode is included in MAM4 on the top of
193 MAM3 to explicitly treat the microphysical ageing of primary carbonaceous aerosols
194 (POM and BC) in the atmosphere. POM and BC in MAM4 are emitted in the primary
195 carbon mode instead of directly in the accumulation mode as in MAM3. MAM4
196 significantly increases the BC and POM concentrations in the remote regions (e.g.,
197 over oceans and Arctic) due to reduced wet scavenging of POM and BC in the
198 primary carbon mode with a lower hygroscopicity than that in the accumulation mode.
199 The increase is relatively small in the land source regions [*Liu et al.*, 2016].
200
201 2.2 Experiment design
202 CAM5 was run with the finite volume dynamics core in a resolution of 0.9°
203 latitude by 1.25° longitude and 30 vertical levels. The model was run for the time
204 period of year 2003 to 2011 (i.e., for 9 years) with prescribed monthly SST and sea
205 ice. The year 2003 was run twice and the first year simulation was used as a model
206 spin-up. Global Fire Emissions Database version 3.1 (GFED 3.1) daily emissions
207 [*Giglio et al.*, 2013] for BC, POM and sulfur dioxide (SO_2) from 2003 to 2011 are
208 prescribed, and the vertical distribution of fire emissions is based on the AeroCom

protocol [*Dentener et al.*, 2006]. Anthropogenic aerosol and precursor gas emissions are from the IPCC AR5 dataset [*Lamarque et al.*, 2010]. We performed our control experiment (FIRE) with the GFED fire emissions turned on and a sensitivity experiment (NOFIRE) with the fire emissions turned off. Differences between FIRE and NOFIRE experiments are used to calculate the REs and atmospheric effects of biomass burning aerosols on temperature and precipitation. Two additional experiments (NOFIREBC and NOFIREPOM) were performed with fire BC and POM emissions turned off, respectively. Differences between the control (FIRE) and these two experiments represent the contribution from biomass burning BC and POM, respectively. Other forcings (e.g., SST, greenhouse gases) of all these experiments are kept the same. We performed ten ensemble members for each of these experiments. Furthermore, we performed the other experiment (FIRE_BBFFBF) using the modified CAM5 model that separately predicts the BC and POM from biomass burning (BB), fossil fuel (FF) and biofuel (BF) sources, while other model features are kept the same as the FIRE experiment. A summary of all the experiments in this study can be found in Table 1.

2.3 Methods of calculating fire aerosol radiative effects

The REs of all fire aerosols, fire BC, and fire POM are calculated from the differences of TOA shortwave fluxes (ΔF) between the FIRE experiment and the three other experiments (NOFIRE, NOFIREBC and NOFIREPOM), respectively. All the atmospheric variables (including temperature, precipitation, and circulation) are

231 allowed to adjust in the experiments. However, with SST and sea ice prescribed in
232 these experiments, only the rapid adjustments are taken into account. Thus the
233 *effective* radiative effects are actually calculated in this study.

234 $$\Delta F_{\text{fire aero}} = F_{\text{fire}} - F_{\text{nofire}} \quad (1)$$

235 $$\Delta F_{\text{fire bc}} = F_{\text{fire}} - F_{\text{nofirebc}} \quad (2)$$

236 $$\Delta F_{\text{fire pom}} = F_{\text{fire}} - F_{\text{nofirepom}} \quad (3)$$

237 The total TOA shortwave flux change can be broken into the REari, REaci, and
238 REsac. The aerosol REaci results from both the aerosol effect on clouds via acting as
239 CCN and the aerosol semi-direct effect on clouds via affecting the atmospheric states
240 due to absorbing aerosols. We adopt the method of *Ghan* [2013] to separate the REari,
241 REaci, and REsac from the total effects of all fire aerosols, fire BC and fire POM,
242 respectively. The method is summarized as follows. F_{clean} is the radiative flux at TOA
243 calculated from a *diagnostic radiation call* in the same control simulations, but
244 neglecting the scattering and absorption of solar radiation by aerosols. $F_{clean,clear}$ is the
245 clear-sky radiative flux at TOA calculated from the same *diagnostic radiation call*,
246 but neglecting scattering and absorption by both clouds and aerosols.

247 $$\Delta F = \underbrace{\Delta(F - F_{clean})}_{\text{(REari)}} + \underbrace{\Delta(F_{clean} - F_{clean,clear})}_{\text{(REaci)}} + \underbrace{\Delta F_{clean,clear}}_{\text{(REsac)}} \quad (4)$$

249 In the method above, REaci includes both aerosol indirect and semi-direct effects.
250 The fire BC has a much weaker indirect effect due to its lower mass burden and lower
251 hygroscopicity compared to fire POM [*Koch et al.*, 2011]. Thus the fire aerosol
252 semi-direct effect can be approximately represented by the REaci of fire BC. The fire

aerosol indirect effect can be estimated as the difference of fire aerosol REaci and semi-direct effect. With the sea ice prescribed in these experiments, the radiative effect of fire aerosols on sea ice albedo is not considered in REsac.

We undertake another method to estimate the fire aerosol REari from the experiment (FIRE_BBFFBF). With explicit predictions of fire POM and fire BC in FIRE_BBFFBF, the REari of fire BC and fire POM are estimated by two diagnostic radiation calls, each time neglecting the scattering and absorption of solar radiation of fire BC and fire POM, respectively. This more direct method is named as BBFFBF, and the REari of fire BC and fire POM will be compared with those from the method of *Ghan* [2013]. The fire BC-in-snow effect is calculated from SNICAR, and compared with the REsac estimated from *Ghan* [2013].

3. Results

3.1 Simulation of biomass burning aerosols

The biomass burning BC and POM from forest, grass and agriculture fires are significant contributors to the total BC and POM emissions. Figure 1 shows the seasonal variation of GFED fire emissions (including forest, grass and agriculture fires) in the global, tropical (25°S to 25°N), and Arctic (60°N to 90°N) regions. Global fire emission is the largest during the boreal summer as well as in the boreal autumn (September/October), when it is the fire season in the tropical regions of the Southern Hemisphere (SH). The tropical fire emission contributes the most to the annual global fire emission (80% for BC and 85% for OC, respectively), compared to

other regions. Arctic is the other important fire region, where the emission maximum is found during the boreal summer. In the boreal summer, the OC emission in the Arctic regions is about 50% of that in the tropical region. The BC emission in the Arctic is much smaller than that of the tropical regions even in the boreal summer fire season. The dominant fire type in the SH tropics is deforestation, savanna and grassland fires, while that in the Arctic is the forest fires. The OC to BC ratio (OC/BC) of forest fires is almost three times higher than that of deforestation, savanna and grassland fires [*van der Werf et al.*, 2010]. This is because for forest fires, most of the emissions come from the smoldering phase of burning, which has a higher OC to BC ratio. For deforestation, savanna and grassland fires, the emissions come mainly from the flaming phase of burning, which yields a lower OC to BC ratio.

Figure S1 in the supplemental materials shows the latitudinal and longitudinal distributions of vertically integrated concentrations (column burdens) of BC and POM from BB, FF, and BF sources based on the FIRE_BBFFBF experiment. The BC and POM from BB source are mainly distributed in the tropical and sub-tropical regions (southern Africa, South America and Southeast Asia) and in the mid- to high latitudes (North of 45°N) of the Northern Hemisphere (NH) (Northeast Asia, Alaska and Canada). The largest column burdens of biomass burning aerosols are located in southern Africa and adjacent oceanic areas (1.5 and 20 mg m^{-2} for BC and POM, respectively). The biomass burning aerosols are important aerosol species in the Arctic regions, and contribute up to 53% and 86% to the total burden of BC and POM in the Arctic (from 60° N to 90°N), respectively. In comparison, the maximum

297 column burdens of fossil fuel BC and POM are found in East Asia, South Asia,
298 Western Europe and North America. The maximum column burdens of biofuel BC
299 and POM occur in East Asia, South Asia and Central Africa. The biofuel and fossil
300 fuel sources are dominant contributors to BC and POM in East Asia and South Asia.
301 In other regions of the world, biomass burning is the primary source of BC and POM.
302 Globally, the biomass burning contributes 41% and 70% to the total burdens of BC
303 and POM, respectively. Biomass burning can also emit SO_2. However, it only
304 contributes ~3% to the total global sulfate burden (figure not shown), so only
305 radiative effects of biomass burning POM and BC are discussed in this study.
306 The simulated aerosol optical depth (AOD) and single scattering albedo (SSA)
307 (including aerosols from all sources) are validated with observations from the
308 AErosol RObotic NETwork (AERONET, http://aeronet.gsfc.nasa.gov) at sites
309 significantly affected by biomass burning activity in southern Africa, South America
310 and the Arctic regions, as shown in Figures 2 and 3 (see Figure S2 in the
311 supplemental materials for the site locations). The AERONET AOD and SSA data are
312 averaged for the years from 2003 to 2011 to match the simulation period, although
313 there are missing AERONET data for some periods. We note that *Tosca et al.* [2013]
314 and *Ward et al.* [2012] applied scaling factors (from 1 to 3 varying by regions) to fire
315 emissions to improve modeled AOD magnitudes, whereas here we do not apply any
316 such scaling. In southern Africa, modeled monthly AOD agrees with observations
317 within a factor of 2 for the three sites (Figure 2a-2c). The underestimation of AOD is
318 found in the tropical site (Mongu) (Figure 2a) during the boreal autumn (the fire

season). The simulated AOD in the two other sites (Skukuza and Ascension Island) is generally consistent with observations in both the magnitude and seasonal trend. The simulated SSA in southern Africa ranges between 0.75 and 0.95 and generally matches the observed SSA magnitude and seasonal cycle in the two land sites (Mongu and Skukuza) (Figure 3a-3b). However, an overestimation of SSA is found in the oceanic site (Ascension Island) (Figure 3c). The reason for this overestimation of SSA and thus the underestimation of absorption AOD (AAOD) is unclear and could be due to that the model has not treated the absorption enhancement of aged fire BC during its transport.

The simulated AOD in South America is generally consistent with observations within a factor of 2 (Figure 2d-2f). The seasonal variation of simulated AOD generally matches the observations. The underestimation of AOD in Alta Floresta and Cuiaba-Miranda is most obvious in September and October (the fire season), which may be attributed to the underestimation of fire emissions. However, the modeled AOD is higher than observations before the fire season for Alta Floresta and Rio Branco, which could be due to the overestimation of fire emission in this period. The simulated SSA in South America ranges mostly between 0.87–0.95 and matches the observations reasonably well (Figure 3d-3f). The modeled SSA is too low during the fire season and exhibits too strong a seasonality. It implies that the model underestimation of scattering aerosols (e.g., POM) may be more severe than that of BC during the fire season.

In the Arctic, small AOD (less than 0.3) and large SSA (larger than 0.9) are

observed for the three sites. The observed large SSA in the fire season (boreal summer) is consistent with the high OC/BC ratio of fire emissions in the Arctic (Figure 1). The model significantly underestimates the observed AOD in the Arctic in both fire and non-fire seasons. The underestimation of AOD can be due to (1) the underestimation of fire emissions in the NH high latitudes [e.g., *Stohl et al.*, 2013] and/or fossil fuel emissions in Asia [e.g., *Cohen and Wang*, 2014], (2) the excessive scavenging of aerosols during their transport from the NH mid-latitude industrial regions by liquid-phase clouds [*Wang et al.*, 2013a], and (3) the coarse horizontal resolution (~100 km) of the model [*Ma et al.*, 2014]. Although MAM4 increases the column burdens of POM and BC by up to 40 % in many remote regions compared to MAM3, it still underestimates the surface BC concentrations in the Arctic [*Liu et al.*, 2016]. The modeled SSA in the Arctic is lower than observations, which implies that the simulation of AAOD is better than that of AOD and the underestimation of non-absorbing aerosols (e.g., sulfate and POM) in the Arctic may be more severe than that of BC.

3.2 Radiative effect due to aerosol-radiation interactions

The annual mean REari of all fire aerosols (including BC, POM and sulfate) estimated with the method of BBFFBF and with the method of *Ghan* [2013] is shown in Figure 4a-4b. The fire sulfate is not included in the calculation of REari of all fire aerosols with the method of BBFFBF. Its effect is minor since the global annual mean burden of fire sulfate (0.09 mg m^{-2}) is much smaller than that of fire POM (1.25 mg

363 m^{-2}), both of which are light-scattering. The statistical significance of REari estimated
364 with the *Ghan* [2013] method over the interannual variability and ensemble member
365 diversity is shown in Figure 4 (and also later figures). The REari of all fire aerosols
366 from the two methods agree with each other very well. Thus, we will report the REari
367 of all fire aerosols with the *Ghan* [2013] method below. The global annual mean
368 REari of all fire aerosols is positive (0.16 ± 0.01 W m^{-2}), which indicates a warming
369 effect from all fire aerosols. The REari is positive on the globe except in some land
370 areas (e.g., southern Africa, South America, Great Lakes, North Canada, and East
371 Siberia). The maximum positive REari is located in ocean areas west of southern
372 Africa (~5.0 W m^{-2}) and South America (~1.5 W m^{-2}). Positive REari up to 1 W m^{-2} is
373 found in the Arctic (60°N to 90°N). The different signs of REari between land and
374 ocean areas of southern Africa and South America result from the differences in cloud
375 fraction and cloud liquid water path (LWP) between land and ocean regions. In the
376 fire season (August-September-October) of the SH tropical regions, cloud fraction
377 and cloud LWP over the land areas (10% and 20 g m^{-2}, respectively) are much smaller
378 than those over the adjacent ocean areas (70% and 70 g m^{-2}, respectively). The
379 biomass burning aerosols are transported above the low-level stratocumulus clouds,
380 and when biomass burning BC resides above clouds, its absorption of solar radiation
381 is significantly enhanced due to the reflection of solar radiation by underlying clouds
382 [*Abel et al.*, 2005; *Zhang et al.*, 2016].

383 A comparison of modeled REari in the boreal autumn
384 (September-October-November) over the South Atlantic Ocean with satellite

observations is shown in Figure 5. The observed above-cloud aerosol REari is calculated with the method of *Zhang et al.* [2014] using the Aqua/MODIS and Terra/MODIS products, respectively. The observed above-cloud aerosol REari over southeastern Atlantic Ocean is 3-12 W m^{-2}, with higher values near the coasts. The simulated REari agrees better with Aqua/MODIS observed REari than with Terra/MODIS in both the magnitude and spatial pattern. REari estimated from Terra/MODIS (morning time) is stronger than the one estimated from Aqua/MODIS (afternoon time) due to the larger amount of underlying clouds in the morning [*Min and Zhang*, 2014]. Over South America during the fire season (August to September), the clear-sky fire aerosol REari is estimated to be -5.2 W m^{-2} by *Sena and Artaxo* [2015], which is larger than our model result (-2.1 W m^{-2}). This is consistent with the underestimation of modeled AOD in South America compared to the AERONET data (Figure 2).

The seasonal variation of REari of all fire aerosols with the *Ghan* [2013] method is shown in the supplemental Figure S3. The REari has a maximum (1.13 W m^{-2}) in the boreal summer (June-July-August, JJA) over the Arctic regions, partially due to the low solar zenith angles there. The maximum positive REari in the tropical regions occurs in the boreal summer and autumn (September, October and November, SON) during the fire season of southern Africa and South America. The REari reaches a positive maximum in Southeast Asia during the fire season in March, April and May (MAM).

The REari of fire BC is shown in Figure 4c-4d. The fire BC REari calculated

from the two methods are similar in magnitudes and spatial patterns, and there is much less noise with the BBFFBF method. The global annual mean fire BC REari is about 0.25 ± 0.01 W m^{-2} and positive over the globe (the regions with negative values in Figure 4d are in general not statistically significant). Unlike all fire aerosols, fire BC generates a positive forcing in the land regions of southern Africa and South America, and the amplification effect of low-level clouds on fire BC positive forcing can be clearly seen in southern Africa and adjacent Atlantic Ocean.

The global annual mean REari of fire POM from the two methods somewhat differs from each other (Figure 4e-4f). The BBFFBF method gives a small negative value (-0.05 W m^{-2}), while the *Ghan* [2013] method shows a small positive value (0.04 ± 0.01 W m^{-2}). The difference is mainly in the Arctic regions where the positive forcing from *Ghan* [2013] is larger than that from the BBFFBF method. This is because the removal of fire POM emissions in the NOFIREPOM experiment affects the properties of aerosol particles within which co-emitted fire BC is internally mixed with fire POM, causing a decrease of BC burden in the Arctic (by ~0.05 mg m^{-2}) compared to the FIRE experiment. Thus, one should be careful in using the *Ghan* [2013] method to diagnose the radiative forcing of a single component within co-emitted aerosols. The REari of fire POM is negative in most of the globe. However, positive forcing can be found over oceanic regions west of southern Africa and South America, North Pacific Ocean and the Polar regions where large amount of low-level clouds, sea ice or land ice exist. The multiple scatterings between the above-cloud fire POM and low-level clouds or between the fire POM and the Earth's bright surface

429 with high albedos could reduce the amount of solar radiation reflected by these
430 low-level clouds and bright surface in the case without the fire POM [*Zhang et al.*,
431 2016]. With the BBFFBF method the sum of REari from fire POM and fire BC (i.e.,
432 0.20 W m^{-2}) is larger than that of all fire aerosols (0.15 W m^{-2}). It reflects the
433 nonlinear interactions among different aerosol components [*Ghan* et al., 2012]. For
434 example, fire POM and water on internally-mixed fire BC particles enhance solar
435 absorption by the fire BC. The nonlinearity is stronger with the *Ghan* [2013] method.
436
437 3.3 Radiative effect due to aerosol-cloud interactions
438 The annual mean REaci due to all fire aerosols, fire BC, and fire POM are shown
439 in Figure 6. The REaci diagnosed with the *Ghan* [2013] method includes both aerosol
440 indirect and semi-direct effects. The fire aerosol semi-direct effect (to be discussed
441 below) is much smaller (-0.04±0.03 W m^{-2} on the global mean) than the indirect
442 effect, and the REaci is mostly from the fire aerosol indirect effect. The global annual
443 mean REaci of all fire aerosols is -0.70±0.05 W m^{-2} (Figure 6a). In the tropical
444 regions, the strong negative REaci is located in the adjacent ocean areas of southern
445 Africa, South America and Australia, with the maximum REaci of -8.0 W m^{-2} over
446 the South Atlantic Ocean. The strong negative REaci also occurs in the Arctic (60°N
447 to 90°N). The REaci in East Siberia, Alaska and Canada is as large as -6.0 W m^{-2}.
448 The fire BC has a weak indirect effect by acting as CCN, but can reduce the cloud
449 amount through its semi-direct effect. The REaci of fire BC (Figure 6b) can
450 approximate the fire BC semi-direct effect with a small global annual mean value of

-0.04±0.03 W m^{-2}. However, stronger positive effect can be found in the western Pacific (3.0 W m^{-2}) and Arctic regions (1.0 W m^{-2}). The global annual mean REaci of fire POM is -0.59±0.03 W m^{-2} (Figure 6c), and dominates the cloud effect of all fire aerosols. The sum of REaci from fire BC and POM (-0.62±0.03 W m^{-2}) is smaller in magnitude than that of all fire aerosols (-0.70±0.05 W m^{-2}) due to the non-linear interactions of fire BC and fire POM [*Jiang et al.*, 2013] as well as the negative REaci of fire sulfate. As an example of the non-linear interactions, the internal mixing of fire POM and fire BC by all fire aerosols enhances the cloud droplet number concentration in comparison to the sum of cloud droplet number concentrations from individual fire POM and fire BC [*Jiang et al.*, 2013].

The seasonal variation of all fire aerosol REaci is shown in Figure 7. The maximum of fire aerosol REaci is in the boreal summer (i.e., the fire season in NH) located in the NH high latitudes (60°N to 90°N). The largest summer REaci is found in the land areas and is as large as -15 W m^{-2}. The fire aerosol REaci in the tropical regions is most significant in the boreal summer (up to -15 W m^{-2}) and autumn (up to -10 W m^{-2}) over the ocean areas. The different spatial distributions of fire aerosol REaci in the NH high latitudes and in the tropics result from the difference in cloud distributions between the two regions. During the fire season the cloud LWP over the land areas in the NH mid- and high latitudes is three times larger than that over the ocean areas in the tropics. Larger cloud LWP favors the stronger REaci, because the larger LWP associated with the warm cloud and rain processes favors the aerosol indirect effect via slowing down the autoconversion of cloud water to rain [*Ghan et*

473 *al.*, 2012; *Jiang et al.*, 2015]. Meanwhile, in the NH high latitudes, the lower solar
474 zenith angle in the boreal summer favors the stronger REaci. Like the fire aerosol
475 REari, the smallest fire aerosol REaci occurs in the boreal spring.

476 Seasonal variations of zonal mean fire aerosol REari, REaci, cloud LWP,
477 low-level (from surface to 750 hPa) cloud amount, and vertically-integrated (burden)
478 concentrations of fire POM and fire BC are shown in Figure 8. The seasonal variation
479 of fire BC and fire POM burdens is largest in the SH low latitudes (from 30°S to 0°N)
480 and NH mid- and high latitudes (50°N to 90°N). Distinct features of these two areas
481 can also be noticed that the maximum fire BC burden in NH (0.3 mg m^{-2}) is much
482 lower than that in SH (0.8 mg m^{-2}), while the maximum POM burdens in these two
483 areas are comparable. Interestingly, the REari is larger in the boreal summer in NH
484 than that in the boreal autumn in SH, although the fire BC burden is much lower in
485 the NH summer. It is mainly due to the larger amount of low clouds in the NH high
486 latitudes, which enhances the absorption of fire BC. The maximum REari in the NH
487 summer is found near the North Pole (70 °N to 90 °N), and not around 60 °N where
488 the fire aerosol burden is highest. The REaci of fire aerosols is about 3 times larger in
489 the boreal summer in NH than that in the boreal autumn in SH, although the burden of
490 fire POM in NH is comparable to that in SH. The larger cloud LWP in the NH
491 summer around 40-70°N favors the stronger REaci there.

492

493 3.4 Surface albedo effect

494 Here we compare the modeled BC-in-snow (BCS) concentrations with

observation data collected from multiple field campaigns over the Arctic [*Doherty et al.*, 2010] and Northern China [*Wang et al.*, 2013b; *Qian et al.*, 2014]. Figure 9a shows the simulated (from FIRE and NOFIRE experiments) and observed BCS concentrations as a function of latitude. The range of observed BCS concentrations is between 1 and 200 ng g^{-1} in the Arctic and between 50 and 2000 ng g^{-1} in Northern China, respectively. Both FIRE and NOFIRE experiments capture the meridional gradient in BCS concentrations between the mid-latitudes (Northern China) and high latitudes (Arctic). The mean and median concentrations of BCS are both overestimated in Northern China, implying the high biases from the anthropogenic emissions and/or model physics (Figure 9b). The mean and median BCS concentrations from the FIRE experiment agree slightly better with observations than those from the NOFIRE experiment in the Arctic (Figure 9b). This suggests that fire emissions are important for BCS concentrations in the Arctic.

The annual mean REsac of all fire aerosols estimated with *Ghan* [2013] and the fire BCS effect diagnosed from SNICAR are shown in Figure 10a. We note that the radiative effect due to BC deposition on sea ice is not considered since sea ice is prescribed in the simulations. The global annual mean REsac (0.03 ± 0.10 W m^{-2}) is much smaller compared to the REari and REaci. The REsac over land is maximum in spring (0.12 ± 0.27 W m^{-2}) and winter (0.06 ± 0.16 W m^{-2}). The REsac over land in summer and autumn is very small (less than 0.01 W m^{-2}). We note that the mean REsac calculated with *Ghan* [2013] is much smaller than the standard deviation resulted from the internal variability.

517 The annual mean fire BCS effect calculated from SNICAR is shown in Figure
518 10b and 10c. The spatial distribution of the fire BCS effect is similar to the fire REsac,
519 implying that the fire REsac has a significant contribution from the fire BCS effect.
520 Averaged when only snow is present, the fire BCS effect is larger (0.048 W m^{-2}). The
521 global mean fire BCS effect (with the presence of snow) can be as large as 0.06 W m^{-2}
522 in spring. The maximum fire BCS effect (up to 1 W m^{-2}) is located in Greenland and
523 the very northern reaches of Canada, while that in the other Arctic regions and North
524 China is smaller.
525 The positive REsac in Siberia, North America and Canada can be a result of BCS
526 effect. However, the REsac in these regions is larger than the BCS effect especially in
527 spring. The snow melting and snow depth change due to the BCS warming may
528 induce a larger positive REsac than the albedo change due to BCS itself. The negative
529 REsac over land can be a result of atmospheric feedbacks caused by fire aerosols
530 [*Ghan*, 2013].
531
532 3.5 Fire aerosol effects on shortwave radiation, global temperature and precipitation
533 Here, we show the annual mean net shortwave flux change at TOA (i.e., total
534 radiative effect), in the atmosphere and at surface, and changes in surface air
535 temperature, convective and large-scale precipitation due to all fire aerosols in Figure
536 11 and Table 2. The global mean net shortwave flux change at TOA due to all fire
537 aerosols is -0.55±0.07 W m^{-2}, which indicates that fire aerosols lead to the reduction
538 of shortwave flux into the Earth's system. The zonal mean TOA shortwave flux

reduction in the Arctic regions (-1.35±1.03 W m^{-2}) is much larger than that in the tropical regions (-0.66±0.09 W m^{-2}). The cooling at TOA is mostly from fire aerosol REaci. The maximum negative RE is located in the land areas of the Arctic and ocean areas of the tropics. Although the global mean total radiative effect is negative, positive effect is found in some land areas (e.g., Africa, Greenland).

The shortwave atmospheric absorption change in the tropical regions is larger than that in the Arctic regions. It is because BC burden in the tropics (0.17 mg m^{-2}) is larger than that in the Arctic (0.09 mg m^{-2}). Strong absorption (~8 W m^{-2}) in the atmosphere is found in the land areas of southern Africa and South America and in the Southeast Atlantic. The surface shortwave flux change in the Arctic is mostly from the TOA shortwave flux reduction due to the fire aerosol REaci, while the surface shortwave flux change in the tropics is mostly due to the fire BC absorption in the atmosphere.

The fire aerosols lead to the reduction of the global mean surface air temperature (T_s) by 0.03±0.03 K, consistent with the reduction of shortwave fluxes at TOA and at surface. The largest surface cooling is found in the Arctic and tropical regions by up to 0.6 K. The cooling of the Arctic is related to the strong fire aerosol REaci, while the cooling in the tropics is mainly from the surface shortwave flux reduction due to the fire BC absorption. The T_s change in the ocean areas is very small since the SST is prescribed in our simulations.

The global mean total precipitation is reduced by 0.010±0.002 mm day^{-1} due to all fire aerosols (Table 2). Unlike the T_s change, the precipitation reduction in the

561 tropics (0.016 ± 0.01 mm day^{-1}) is much larger than that in the Arctic (0.001 ± 0.02
562 mm day^{-1}, not statistically significant). The reduction in the tropics is mainly from the
563 large-scale precipitation decrease (0.015 ± 0.003 mm day^{-1}). The net decrease in the
564 convective precipitation is very small in the tropics (0.001 ± 0.009 mm day^{-1}, not
565 statistically significant), as the convective precipitation is significantly decreased near
566 the equator and increased in the regions away from the equator, partly consistent with
567 the results of *Tosca et al.* [2013]. The precipitation reduction in southern Africa is
568 consistent with the recent findings of *Hodnebrog et al.* [2016]. The shortwave flux
569 reduction at surface leads to a stabilization of the atmospheric boundary layer and a
570 suppression of the convection near the equator. The strong atmospheric absorption by
571 fire BC leads to the reduction of low-level clouds and large-scale precipitation in the
572 tropics. Both effects lead to a significant reduction of total precipitation near the
573 equator. The precipitation decrease in the NH high latitudes is mainly from the
574 reduction of convective precipitation. We note that the temperature and (especially)
575 precipitation changes reported here do not represent the complete impact of fire
576 aerosols, since the SSTs are fixed in our simulations. Fully-coupled atmosphere and
577 ocean models will be used to further investigate the impact of fire aerosols.

578 Figure 12 shows the changes of T_s, total precipitation, cloud LWP, and low-level
579 cloud cover in the summer due to all fire aerosols. The T_s is reduced by more than 1 K
580 in most of land areas around 60°N. The maximum cooling (larger than 1.5 K) is found
581 in East Siberia, Alaska and Canada. A decrease of total precipitation (by about 0.2
582 mm day^{-1}) is found in these regions. Accompanying the surface cooling and

precipitation reduction, a significant increase of cloud LWP and low-level cloud cover is found there. This is a result of the indirect effect of fire aerosols in the land areas of the Arctic (60°N to 90°N). The fire POM leads to the reduction of cloud droplet effective radius and the increase of cloud droplet number concentration, consistent with observed fire effects on clouds in Canada and the United States [*Peng et al.*, 2002].

4. Discussion and Conclusions

Although many studies have been conducted on the fire aerosol RE and RF [e.g., *Bond et al.*, 2013; *Myhre et al.*, 2013b; *Ward et al.*, 2012; *Tosca et al.*, 2013], the current estimations are still associated with large uncertainties. In this study, the fire aerosol RE (including REari, REaci and REsac) is calculated based on a new method from *Ghan* [2013]. In addition, the fire aerosol REari and fire BC-in-snow effect are diagnosed from an experiment of CESM which tracks the open fire BC and POM separately from fossil fuel and biofuel sources and compared with the estimates from the *Ghan* [2013] method.

The BC and POM burdens from open fires are largest in the tropical regions (southern Africa, South America and Southeast Asia) and in the NH mid- to high latitudes (North of 45°N) (Northeast Asia, Alaska and Canada). Fire aerosols contribute 41% and 70% to the global burden of BC and POM, respectively. When comparing with the AERONET AOD and SSA data, modeled monthly AOD agrees with observations within a factor of 2 for most of the southern African and South

American sites. The model underestimation of AOD is found in the South American sites near fire source regions, which is most obvious in the fire season (September and October). The model underestimates the observed AOD in the Arctic regions in both fire and non-fire seasons. The modeled SSA in southern Africa and South America is generally in agreement with observations, while the modeled SSA in the Arctic is lower.

The annual mean REari of all fire aerosols is 0.16 ± 0.01 W m^{-2} and positive over most areas except in some land areas (e.g., southern Africa, North Canada, and East Siberia). The annual maximum REari is found in the oceanic areas west of southern Africa (5 W m^{-2}) and South America (1.5 W m^{-2}). The positive REari over the land regions of southern Africa and South America is smaller, although the fire aerosol burdens are higher. The annual zonal mean REari in the Arctic regions can reach 0.43 ± 0.028 W m^{-2}, and is larger than that in the tropical regions (0.17 ± 0.017 W m^{-2}), although the fire aerosol burden is higher in the tropics. The annual mean REari of fire BC is about 0.25 ± 0.01 W m^{-2} and positive over the globe. Fire POM induces a weak negative REari globally (-0.05 W m^{-2}) with the BBFFBF method and a small positive value (0.04 ± 0.01 W m^{-2}) with the *Ghan* [2013] method. The positive REari of fire POM is found over oceanic areas west of southern Africa and South America, North Pacific, and polar regions where the low-level cloud coverage is large or the surface albedo is higher.

The global annual mean REaci of all fire aerosols is -0.70 ± 0.05 W m^{-2} and the maximum effect is located in the ocean areas west of southern Africa and South

America and land areas of the NH high latitudes. The maximum fire aerosol REaci occurs in the NH high latitudes in the boreal summer, which results from the large cloud LWP over the land areas and the low solar zenith angle. Associated with the strong indirect effects of fire aerosols in the Arctic summer, significant surface cooling, precipitation reduction, and low-level cloud cover increase are found in these regions.

Modeled BCS concentrations from the FIRE experiment are evaluated against observations in Northern China and in the Arctic, and generally agree with the observations for the mean and median values in the Arctic regions. The high bias of modeled BCS concentrations in Northern China may not result from the fire BC because differences in BCS concentrations between FIRE and NOFIRE experiments are very small in North China. The global annual mean REsac is 0.03 ± 0.10 W m^{-2} (statistically insignificant) with the maximum effect in spring (0.12 W m^{-2}). The REsac is mainly due to the effect of fire BC deposit on snow (0.02 W m^{-2}) diagnosed from SNICAR with the maximum effect as large as 0.06 W m^{-2} (when snow is present) in spring.

The fire aerosols reduce the global mean surface air temperature (T_s) by 0.03 ± 0.03 K and precipitation by 0.01 ± 0.002 mm day^{-1}. The maximum cooling (~1 K) due to fire aerosols occurs around 60°N in summer, and a suppression of precipitation (~0.1 mm day^{-1}) is also found there. The strong cooling is a result of the strong indirect effects (-15 W m^{-2}) in the land areas of the Arctic regions (60°N to 90°N). A significant reduction of precipitation in southern Africa is also noticed. We note that

649 these results are based on the simulations with fixed SSTs and may not represent the
650 full climate responses.

651 In our study, the global radiative effect of fire aerosols is estimated from
652 simulations performed with the 4-mode version Modal aerosol module (MAM4) [*Liu*
653 *et al.*, 2016], daily fire emissions with prescribed vertical emission profiles, and
654 higher model resolution (0.9° by 1.25°) compared to earlier modeling studies of fire
655 aerosols [*Tosca et al.*, 2013; *Ward et al.*, 2012]. In their studies, the GFED fire
656 aerosol emissions were increased by a factor of 1-3 depending on regions to match the
657 observed AOD. In our study, we do not apply the scaling factor to the fire aerosol
658 emissions. Our global annual mean REari of fire aerosols (0.16 ± 0.01 W m^{-2}) is,
659 however, close to 0.18 W m^{-2} in *Tosca et al.* [2013] and 0.13 W m^{-2} in *Ward et al.*
660 [2012]. The similar fire aerosol REari from our study but with smaller fire emissions
661 than these previous studies can result from (1) the use of MAM4 in our study which
662 more realistically represents the external/internal mixing of BC with other soluble
663 aerosol species; (2) the more accurate estimation of REari of fire aerosols in the
664 presence of low-level clouds with the method of *Ghan* [2013]; and (3) the inclusion of
665 vertical emissions of fire aerosols, which allows more efficient transport of fire
666 aerosols from sources. The REaci due to fire aerosols in our study (-0.70 ± 0.05 W m^{-2})
667 is smaller than -1.64 W m^{-2} in *Ward et al.* [2012] due to the lower fire POM emissions
668 used in this study compared to *Ward et al.* [2012].

669 We note that there are limitations and uncertainties with our study. The model
670 still underestimates observed AODs (mostly within a factor of 2) at the sites

671 predominantly influenced by biomass burning aerosols during the fire season, which
672 implies that the fire aerosol radiative forcing can be stronger than estimated in this
673 study. The RE estimates of fire POM and fire BC with the *Ghan* [2013] approach may
674 not be accurate due to the internal mixing of co-emitted fire components (POM and
675 BC). In our simulations, sea ice is prescribed, and thus the fire BC effect on sea ice
676 albedo is not considered. The brown carbon component of POM [*Feng et al.*, 2013] is
677 not treated in the current CESM model, which may result in an underestimation of
678 atmospheric absorption of fire aerosols.
679
680 **Acknowledgments**
681 This work is supported by the Office of Science of the US Department of Energy
682 (DOE) as the NSF-DOE-USDA Joint Earth System Modeling (EaSM) Program, the
683 National Key Basic Research Program (973 Program) of China under Grant No.
684 2010CB428504, and the National Natural Science Foundation of China (NSFC) under
685 Grant No.41505062. The Pacific Northwest National Laboratory is operated for the
686 DOE by the Battelle Memorial Institute under contract DE-AC05-76RL01830. The
687 authors would like to acknowledge the use of computational resources
688 (ark:/85065/d7wd3xhc) at the NCAR-Wyoming Supercomputing Center provided by
689 the National Science Foundation and the State of Wyoming, and supported by
690 NCAR's Computational and Information Systems Laboratory. The fire emission data
691 were obtained from the Global Fire Emissions Database (GFED,
692 http://www.globalfiredata.org). The AERONET data were obtained from
693 http://aeronet.gsfc.nasa.gov. We thank Xiangjun Shi for the help with processing the

AERONET data.

References

Abel, S. J., Highwood, E. J., Haywood, J. M., and Stringer, M. A.: The direct radiative effect of biomass burning aerosols over southern Africa, Atmos. Chem. Phys., 5, 1999-2018, 10.5194/acp-5-1999-2005, 2005.

Ackerman, A. S., Toon, O. B., Stevens, D. E., Heymsfield, A. J., Ramanathan, V., and Welton, E. J.: Reduction of Tropical Cloudiness by Soot, Science, 288, 1042-1047, 10.1126/science.288.5468.1042, 2000.

Andreae, M. O., and Rosenfeld, D.: Aerosol–cloud–precipitation interactions. Part 1. The nature and sources of cloud-active aerosols, Earth-Science Reviews, 89, 13-41, http://dx.doi.org/10.1016/j.earscirev.2008.03.001, 2008.

Andreae, M. O., Rosenfeld, D., Artaxo, P., Costa, A. A., Frank, G. P., Longo, K. M., and Silva-Dias, M. A. F.: Smoking Rain Clouds over the Amazon, Science, 303, 1337-1342, 10.1126/science.1092779, 2004.

Bistinas, I., Harrison, S. P., Prentice, I. C., and Pereira, J. M. C.: Causal relationships versus emergent patterns in the global controls of fire frequency, Biogeosciences, 11, 5087-5101, 10.5194/bg-11-5087-2014, 2014.

Bond, T. C., Doherty, S. J., Fahey, D. W., Forster, P. M., Berntsen, T., DeAngelo, B. J., Flanner, M. G., Ghan, S., Karcher, B., Koch, D., Kinne, S., Kondo, Y., Quinn, P. K., Sarofim, M. C., Schultz, M. G., Schulz, M., Venkataraman, C., Zhang, H., Zhang, S., Bellouin, N., Guttikunda, S. K., Hopke, P. K., Jacobson, M. Z., Kaiser, J. W., Klimont, Z., Lohmann, U., Schwarz, J. P., Shindell, D., Storelvmo, T., Warren, S. G., and Zender, C. S.: Bounding the role of black carbon in the climate system: A scientific assessment, J Geophys Res-Atmos, 118, 5380-5552, Doi 10.1002/Jgrd.50171, 2013.

Boucher, O., and Tanré, D.: Estimation of the aerosol perturbation to the Earth's Radiative Budget over oceans using POLDER satellite aerosol retrievals, Geophysical Research Letters, 27, 1103-1106, 10.1029/1999GL010963, 2000.

724 Bowman, D. M. J. S., Balch, J. K., Artaxo, P., Bond, W. J., Carlson, J. M., Cochrane,
725 M. A., D'Antonio, C. M., DeFries, R. S., Doyle, J. C., Harrison, S. P., Johnston, F.
726 H., Keeley, J. E., Krawchuk, M. A., Kull, C. A., Marston, J. B., Moritz, M. A.,
727 Prentice, I. C., Roos, C. I., Scott, A. C., Swetnam, T. W., van der Werf, G. R., and
728 Pyne, S. J.: Fire in the Earth System, Science, 324, 481-484,
729 10.1126/science.1163886, 2009.
730 Carslaw, K. S., Boucher, O., Spracklen, D. V., Mann, G. W., Rae, J. G. L., Woodward,
731 S., and Kulmala, M.: A review of natural aerosol interactions and feedbacks
732 within the Earth system, Atmos. Chem. Phys., 10, 1701-1737,
733 10.5194/acp-10-1701-2010, 2010.
734 Chakrabarty, R. K., Beres, N. D., Moosmüller, H., China, S., Mazzoleni, C., Dubey,
735 M. K., Liu, L., and Mishchenko, M. I.: Soot superaggregates from flaming
736 wildfires and their direct radiative forcing, Scientific Reports, 4, 5508,
737 10.1038/srep05508.
738 Ciais, P., Sabine, C., Bala, G., Bopp, L., Brovkin, V., Canadell, J., Chhabra, A.,
739 DeFries, R., Galloway, J., Heimann, M., Jones, C., Le Quéré, C., Myneni, R. B.,
740 Piao, S., and Thornton, P.: Carbon and Other Biogeochemical Cycles, in: Climate
741 Change 2013: The Physical Science Basis. Contribution of Working Group I to
742 the Fifth Assessment Report of the Intergovernmental Panel on Climate Change,
743 edited by: Stocker, T. F., Qin, D., Plattner, G.-K., Tignor, M., Allen, S. K.,
744 Boschung, J., Nauels, A., Xia, Y., Bex, V., and Midgley, P. M., Cambridge
745 University Press, Cambridge, United Kingdom and New York, NY, USA, 465–
746 570, 2013.
747 Cohen, J. B., and Wang, C.: Estimating global black carbon emissions using a
748 top-down Kalman Filter approach, Journal of Geophysical Research: Atmospheres,
749 119, 2013JD019912, 10.1002/2013JD019912, 2014.
750 Dentener, F., Kinne, S., Bond, T., Boucher, O., Cofala, J., Generoso, S., Ginoux, P.,
751 Gong, S., Hoelzemann, J. J., Ito, A., Marelli, L., Penner, J. E., Putaud, J. P.,
752 Textor, C., Schulz, M., van der Werf, G. R., and Wilson, J.: Emissions of primary
753 aerosol and precursor gases in the years 2000 and 1750 prescribed data-sets for

754 AeroCom, Atmos. Chem. Phys., 6, 4321-4344, 10.5194/acp-6-4321-2006, 2006.
755 Doherty, S. J., Warren, S. G., Grenfell, T. C., Clarke, A. D., and Brandt, R. E.:
756 Light-absorbing impurities in Arctic snow, Atmos. Chem. Phys., 10, 11647-11680,
757 10.5194/acp-10-11647-2010, 2010.
758 Feng, Y., V. Ramanathan, and V. R. Kotamarthi: Brown carbon: a significant
759 atmospheric absorber of solar radiation?, Atmos. Chem. Phys., 13(17), 8607–8621,
760 doi:10.5194/acp-13-8607-2013, 2013.
761 Flanner, M. G., and Zender, C. S.: Snowpack radiative heating: Influence on Tibetan
762 Plateau climate, Geophysical Research Letters, 32, L06501, Artn L06501, Doi
763 10.1029/2004gl022076, 2005.
764 Flanner, M. G., Zender, C. S., Randerson, J. T., and Rasch, P. J.: Present-day climate
765 forcing and response from black carbon in snow, Journal of Geophysical Research:
766 Atmospheres, 112, D11202, 10.1029/2006JD008003, 2007.
767 Flanner, M. G., Zender, C. S., Hess, P. G., Mahowald, N. M., Painter, T. H.,
768 Ramanathan, V., and Rasch, P. J.: Springtime warming and reduced snow cover
769 from carbonaceous particles, Atmos. Chem. Phys., 9, 2481-2497,
770 10.5194/acp-9-2481-2009, 2009.
771 Forster, P., Ramaswamy, V., Artaxo, P., Berntsen, T., Betts, R., Fahey, D. W.,
772 Haywood, J., Lean, J., Lowe, D. C., and Myhre, G.: Changes in atmospheric
773 constituents and in radiative forcing. Chapter 2, in: Climate Change 2007. The
774 Physical Science Basis, 2007.
775 Ghan, S. J.: Technical Note: Estimating aerosol effects on cloud radiative forcing,
776 Atmos. Chem. Phys., 13, 9971-9974, 10.5194/acp-13-9971-2013, 2013.
777 Ghan, S. J., Liu, X., Easter, R. C., Zaveri, R., Rasch, P. J., Yoon, J.-H., and Eaton, B.:
778 Toward a Minimal Representation of Aerosols in Climate Models: Comparative
779 Decomposition of Aerosol Direct, Semidirect, and Indirect Radiative Forcing,
780 Journal of Climate, 25, 6461-6476, doi:10.1175/JCLI-D-11-00650.1, 2012.
781 Giglio, L., Randerson, J. T., and van der Werf, G. R.: Analysis of daily, monthly, and
782 annual burned area using the fourth-generation global fire emissions database
783 (GFED4), Journal of Geophysical Research: Biogeosciences, 118, 317-328,

784 10.1002/jgrg.20042, 2013.
785 Hansen, J., Sato, M., Ruedy, R., Nazarenko, L., Lacis, A., Schmidt, G. A., Russell, G.,
786 Aleinov, I., Bauer, M., Bauer, S., Bell, N., Cairns, B., Canuto, V., Chandler, M.,
787 Cheng, Y., Del Genio, A., Faluvegi, G., Fleming, E., Friend, A., Hall, T., Jackman,
788 C., Kelley, M., Kiang, N., Koch, D., Lean, J., Lerner, J., Lo, K., Menon, S., Miller,
789 R., Minnis, P., Novakov, T., Oinas, V., Perlwitz, J., Perlwitz, J., Rind, D.,
790 Romanou, A., Shindell, D., Stone, P., Sun, S., Tausnev, N., Thresher, D., Wielicki,
791 B., Wong, T., Yao, M., and Zhang, S.: Efficacy of climate forcings, Journal of
792 Geophysical Research: Atmospheres, 110, D18104, 10.1029/2005JD005776,
793 2005.
794 Heald, C. L., Ridley, D. A., Kroll, J. H., Barrett, S. R. H., Cady-Pereira, K. E.,
795 Alvarado, M. J., and Holmes, C. D.: Contrasting the direct radiative effect and
796 direct radiative forcing of aerosols, Atmos. Chem. Phys., 14, 5513-5527,
797 10.5194/acp-14-5513-2014, 2014.
798 Houghton, J. T.: Climate change 1995: The science of climate change: contribution of
799 working group I to the second assessment report of the Intergovernmental Panel
800 on Climate Change, Cambridge University Press, 1996.
801 IPCC (2013), Climate Change 2013: The Physical Science Basis. Contribution of
802 Working Group I to the Fifth Assessment Report of the Intergovernmental Panel
803 on Climate Change, 1535 pp., Cambridge University Press, Cambridge, United
804 Kingdom and New York, NY, USA, doi:10.1017/CBO9781107415324.
805 Jacobson, M. Z.: Climate response of fossil fuel and biofuel soot, accounting for
806 soot's feedback to snow and sea ice albedo and emissivity, Journal of Geophysical
807 Research: Atmospheres, 109, D21201, 10.1029/2004JD004945, 2004.
808 Jiang, Y., Liu, X., Yang, X.-Q., and Wang, M.: A numerical study of the effect of
809 different aerosol types on East Asian summer clouds and precipitation,
810 Atmospheric Environment, 70, 51-63,
811 http://dx.doi.org/10.1016/j.atmosenv.2012.12.039, 2013.
812 Jiang, Y., Yang, X.-Q., and Liu, X.: Seasonality in anthropogenic aerosol effects on
813 East Asian climate simulated with CAM5, Journal of Geophysical Research:

814 Atmospheres, 120, 2015JD023451, 10.1002/2015JD023451, 2015.
815 Jones, A., Haywood, J. M., and Boucher, O.: Aerosol forcing, climate response and
816 climate sensitivity in the Hadley Centre climate model, Journal of Geophysical
817 Research: Atmospheres, 112, D20211, 10.1029/2007JD008688, 2007.
818 Kaiser, J. W., Heil, A., Andreae, M. O., Benedetti, A., Chubarova, N., Jones, L.,
819 Morcrette, J. J., Razinger, M., Schultz, M. G., Suttie, M., and van der Werf, G. R.:
820 Biomass burning emissions estimated with a global fire assimilation system based
821 on observed fire radiative power, Biogeosciences, 9, 527-554,
822 10.5194/bg-9-527-2012, 2012.
823 Keywood, M., Kanakidou, M., Stohl, A., Dentener, F., Grassi, G., Meyer, C. P.,
824 Torseth, K., Edwards, D., Thompson, A. M., Lohmann, U., and Burrows, J.: Fire
825 in the Air: Biomass Burning Impacts in a Changing Climate, Critical Reviews in
826 Environmental Science and Technology, 43, 40-83,
827 10.1080/10643389.2011.604248, 2011.
828 Koch, D., Menon, S., Del Genio, A., Ruedy, R., Alienov, I., and Schmidt, G. A.:
829 Distinguishing Aerosol Impacts on Climate over the Past Century, Journal of
830 Climate, 22, 2659-2677, 10.1175/2008JCLI2573.1, 2009.
831 Koch, D., Balkanski, Y., Bauer, S. E., Easter, R. C., Ferrachat, S., Ghan, S. J., Hoose,
832 C., Iversen, T., Kirkevåg, A., Kristjansson, J. E., Liu, X., Lohmann, U., Menon, S.,
833 Quaas, J., Schulz, M., Seland, Ø., Takemura, T., and Yan, N.: Soot microphysical
834 effects on liquid clouds, a multi-model investigation, Atmos. Chem. Phys., 11,
835 1051-1064, 10.5194/acp-11-1051-2011, 2011.
836 Koch, D., and Del Genio, A. D.: Black carbon semi-direct effects on cloud cover:
837 review and synthesis, Atmos. Chem. Phys., 10, 7685-7696,
838 10.5194/acp-10-7685-2010, 2010.
839 Koren, I., Kaufman, Y. J., Rosenfeld, D., Remer, L. A., and Rudich, Y.: Aerosol
840 invigoration and restructuring of Atlantic convective clouds, Geophysical
841 Research Letters, 32, L14828, 10.1029/2005GL023187, 2005.
842 Lamarque, J. F., Bond, T. C., Eyring, V., Granier, C., Heil, A., Klimont, Z., Lee, D.,
843 Liousse, C., Mieville, A., Owen, B., Schultz, M. G., Shindell, D., Smith, S. J.,

844 Stehfest, E., Van Aardenne, J., Cooper, O. R., Kainuma, M., Mahowald, N.,
845 McConnell, J. R., Naik, V., Riahi, K., and van Vuuren, D. P.: Historical (1850–
846 2000) gridded anthropogenic and biomass burning emissions of reactive gases and
847 aerosols: methodology and application, Atmos. Chem. Phys., 10, 7017-7039,
848 10.5194/acp-10-7017-2010, 2010.
849 Liu, X., J. E. Penner, B. Das, D. Bergmann, J. M. Rodriguez, S. Strahan, M. Wang
850 and Y. Feng: Uncertainties in global aerosol simulations: Assessment using three
851 meteorological datasets, Journal of Geophysical Research, 112, D11212,
852 doi:10.1029/2006JD008216, 2007.
853 Liu, X., Easter, R. C., Ghan, S. J., Zaveri, R., Rasch, P., Shi, X., Lamarque, J. F.,
854 Gettelman, A., Morrison, H., Vitt, F., Conley, A., Park, S., Neale, R., Hannay, C.,
855 Ekman, A. M. L., Hess, P., Mahowald, N., Collins, W., Iacono, M. J., Bretherton,
856 C. S., Flanner, M. G., and Mitchell, D.: Toward a minimal representation of
857 aerosols in climate models: description and evaluation in the Community
858 Atmosphere Model CAM5, Geosci. Model Dev., 5, 709-739,
859 10.5194/gmd-5-709-2012, 2012.
860 Liu, X., Ma, P. L., Wang, H., Tilmes, S., Singh, B., Easter, R. C., Ghan, S. J., and
861 Rasch, P. J.: Description and evaluation of a new four-mode version of the Modal
862 Aerosol Module (MAM4) within version 5.3 of the Community Atmosphere
863 Model, Geosci. Model Dev., 9, 505-522, 10.5194/gmd-9-505-2016, 2016.
864 Liu, Y.: Atmospheric response and feedback to radiative forcing from biomass
865 burning in tropical South America, Agricultural and Forest Meteorology, 133,
866 40-53, http://dx.doi.org/10.1016/j.agrformet.2005.03.011, 2005.
867 Liu, Y., Goodrick, S., and Heilman, W.: Wildland fire emissions, carbon, and climate:
868 Wildfire–climate interactions, Forest Ecology and Management, 317, 80-96,
869 http://dx.doi.org/10.1016/j.foreco.2013.02.020, 2014.
870 Lu, Z., and Sokolik, I. N.: The effect of smoke emission amount on changes in cloud
871 properties and precipitation: A case study of Canadian boreal wildfires of 2007,
872 Journal of Geophysical Research: Atmospheres, 118, 2013JD019860,
873 10.1002/2013JD019860, 2013.

874 Ma, P.-L., P. J. Rasch, H. Wang, K. Zhang, R. C. Easter, S. Tilmes, J. D. Fast, X. Liu,
875 J.-H. Yoon, and J.-F. Lamarque: The role of circulation features on black carbon
876 transport into the Arctic in the Community Atmosphere Model version 5 (CAM5),
877 J. Geophys. Res. Atmos., 118, 4657–4669, 2013.
878 Ma, P. L., Rasch, P. J., Fast, J. D., Easter, R. C., Gustafson Jr, W. I., Liu, X., Ghan, S.
879 J., and Singh, B.: Assessing the CAM5 physics suite in the WRF-Chem model:
880 implementation, resolution sensitivity, and a first evaluation for a regional case
881 study, Geosci. Model Dev., 7, 755-778, 10.5194/gmd-7-755-2014, 2014.
882 Ma, P.-L., P. J. Rasch, M. Wang, H. Wang, S. J. Ghan, R. C. Easter, W. I. Gustafson
883 Jr., X. Liu, Y. Zhang, and H.-Y. Ma: How does increasing horizontal resolution in
884 a global climate model improve the simulation of aerosol-cloud interactions?,
885 Geophys. Res. Lett., 42, 5058–5065, doi:10.1002/2015GL064183, 2015.
886 Marlon, J. R., Bartlein, P. J., Walsh, M. K., Harrison, S. P., Brown, K. J., Edwards, M.
887 E., Higuera, P. E., Power, M. J., Anderson, R. S., Briles, C., Brunelle, A.,
888 Carcaillet, C., Daniels, M., Hu, F. S., Lavoie, M., Long, C., Minckley, T., Richard,
889 P. J. H., Scott, A. C., Shafer, D. S., Tinner, W., Umbanhowar, C. E., and Whitlock,
890 C.: Wildfire responses to abrupt climate change in North America, Proceedings of
891 the National Academy of Sciences, 106, 2519-2524, 10.1073/pnas.0808212106,
892 2009.
893 McCarthy, J. J.: Climate change 2001: impacts, adaptation, and vulnerability:
894 contribution of Working Group II to the third assessment report of the
895 Intergovernmental Panel on Climate Change, Cambridge University Press, 2001.
896 Min M., and Zhang Z.: On the influence of cloud fraction diurnal cycle and sub-grid
897 cloud optical thickness variability on all-sky direct aerosol radiative forcing, J.
898 Quant. Spectros. Radiat. Transfer, doi:10.1016/j.jqsrt.2014.03.014, 2014.
899 Morrison, H., and Gettelman, A.: A New Two-Moment Bulk Stratiform Cloud
900 Microphysics Scheme in the Community Atmosphere Model, Version 3 (CAM3).
901 Part I: Description and Numerical Tests, Journal of Climate, 21, 3642-3659,
902 doi:10.1175/2008JCLI2105.1, 2008.
903 Myhre, G., Samset, B. H., Schulz, M., Balkanski, Y., Bauer, S., Berntsen, T. K., Bian,

H., Bellouin, N., Chin, M., Diehl, T., Easter, R. C., Feichter, J., Ghan, S. J., Hauglustaine, D., Iversen, T., Kinne, S., Kirkevåg, A., Lamarque, J. F., Lin, G., Liu, X., Lund, M. T., Luo, G., Ma, X., van Noije, T., Penner, J. E., Rasch, P. J., Ruiz, A., Seland, Ø., Skeie, R. B., Stier, P., Takemura, T., Tsigaridis, K., Wang, P., Wang, Z., Xu, L., Yu, H., Yu, F., Yoon, J. H., Zhang, K., Zhang, H., and Zhou, C.: Radiative forcing of the direct aerosol effect from AeroCom Phase II simulations, Atmos. Chem. Phys., 13, 1853-1877, 10.5194/acp-13-1853-2013, 2013.

Myhre, G., Shindell, D., Bréon, F.-M., Collins, W., Fuglestvedt, J., Huang, J., Koch, D., Lamarque, J.-F., Lee, D., Mendoza, B., Nakajima, T., Robock, A., Stephens, G., Takemura, T., and Zhang, H.: Anthropogenic and Natural Radiative Forcing, in: Climate Change 2013: The Physical Science Basis. Contribution of Working Group I to the Fifth Assessment Report of the Intergovernmental Panel on Climate Change, edited by: Stocker, T. F., Qin, D., Plattner, G.-K., Tignor, M., Allen, S. K., Boschung, J., Nauels, A., Xia, Y., Bex, V., and Midgley, P. M., Cambridge University Press, Cambridge, United Kingdom and New York, NY, USA, 659–740, 2013.

Myhre, G., and Samset, B. H.: Standard climate models radiation codes underestimate black carbon radiative forcing, Atmos. Chem. Phys., 15, 2883-2888, 10.5194/acp-15-2883-2015, 2015.

Neale, R., Chen, C., Gettelman, A., Lauritzen, P., Park, S., Williamson, D., Garcia, R., Kinnison, D., Lamarque, J., and Marsh, D.: Description of the NCAR Community Atmosphere Model (CAM 5.0), 2010.

Oleson, K. W., Lawrence, D. M., Gordon, B., Flanner, M. G., Kluzek, E., Peter, J., Levis, S., Swenson, S. C., Thornton, E., and Feddema, J.: Technical description of version 4.0 of the Community Land Model (CLM), 2010.

Peng, Y., Lohmann, U., Leaitch, R., Banic, C., and Couture, M.: The cloud albedo-cloud droplet effective radius relationship for clean and polluted clouds from RACE and FIRE.ACE, Journal of Geophysical Research: Atmospheres, 107, AAC 1-1-AAC 1-6, 10.1029/2000JD000281, 2002.

934 Qian, Y., Flanner, M. G., Leung, L. R., and Wang, W.: Sensitivity studies on the
935 impacts of Tibetan Plateau snowpack pollution on the Asian hydrological cycle
936 and monsoon climate, Atmos. Chem. Phys., 11, 1929-1948,
937 10.5194/acp-11-1929-2011, 2011.
938 Qian, Y., Gong, D., Fan, J., Leung, L. R., Bennartz, R., Chen, D., and Wang, W.:
939 Heavy pollution suppresses light rain in China: Observations and modeling,
940 Journal of Geophysical Research: Atmospheres, 114, D00K02,
941 10.1029/2008JD011575, 2009.
942 Qian, Y., Wang, H., Zhang, R., Flanner, M. G., and Rasch, P. J.: A sensitivity study
943 on modeling black carbon in snow and its radiative forcing over the Arctic and
944 Northern China, Environmental Research Letters, 9, 064001,
945 10.1088/1748-9326/9/6/064001, 2014.
946 Qian, Y., Yasunari, T. J., Doherty, S. J., Flanner, M. G., Lau, W. K. M., Ming, J.,
947 Wang, H., Wang, M., Warren, S. G., and Zhang, R.: Light-absorbing particles in
948 snow and ice: Measurement and modeling of climatic and hydrological impact,
949 Advances in Atmospheric Sciences, 32, 64-91, 10.1007/s00376-014-0010-0,
950 2015.
951 Quinn, P. K., Bates, T. S., Baum, E., Doubleday, N., Fiore, A. M., Flanner, M.,
952 Fridlind, A., Garrett, T. J., Koch, D., Menon, S., Shindell, D., Stohl, A., and
953 Warren, S. G.: Short-lived pollutants in the Arctic: their climate impact and
954 possible mitigation strategies, Atmos. Chem. Phys., 8, 1723-1735,
955 10.5194/acp-8-1723-2008, 2008.
956 Randerson, J. T., Liu, H., Flanner, M. G., Chambers, S. D., Jin, Y., Hess, P. G.,
957 Pfister, G., Mack, M. C., Treseder, K. K., Welp, L. R., Chapin, F. S., Harden, J.
958 W., Goulden, M. L., Lyons, E., Neff, J. C., Schuur, E. A. G., and Zender, C. S.:
959 The Impact of Boreal Forest Fire on Climate Warming, Science, 314, 1130-1132,
960 2006.
961 Rypdal, K., Rive, N., Berntsen, T. K., Klimont, Z., Mideksa, T. K., Myhre, G., and
962 Skeie, R. B.: Costs and global impacts of black carbon abatement strategies,
963 Tellus B, 61, 625-641, 10.1111/j.1600-0889.2009.00430.x, 2009.

964 Sena, E. T., and Artaxo, P.: A novel methodology for large-scale daily assessment of
965 the direct radiative forcing of smoke aerosols, Atmospheric Chemistry and
966 Physics, 15, 5471-5483, 10.5194/acp-15-5471-2015, 2015.
967 Skeie, R. B., Berntsen, T., Myhre, G., Pedersen, C. A., Ström, J., Gerland, S., and
968 Ogren, J. A.: Black carbon in the atmosphere and snow, from pre-industrial times
969 until present, Atmos. Chem. Phys., 11, 6809-6836, 10.5194/acp-11-6809-2011,
970 2011.
971 Sommers, W. T., Loehman, R. A., and Hardy, C. C.: Wildland fire emissions, carbon,
972 and climate: Science overview and knowledge needs, Forest Ecology and
973 Management, 317, 1-8, http://dx.doi.org/10.1016/j.foreco.2013.12.014, 2014.
974 Stohl, A., Klimont, Z., Eckhardt, S., Kupiainen, K., Shevchenko, V. P., Kopeikin, V.
975 M., and Novigatsky, A. N.: Black carbon in the Arctic: the underestimated role of
976 gas flaring and residential combustion emissions, Atmos. Chem. Phys., 13,
977 8833-8855, 10.5194/acp-13-8833-2013, 2013.
978 Tosca, M. G., Diner, D. J., Garay, M. J., and Kalashnikova, O. V.: Observational
979 evidence of fire-driven reduction of cloud fraction in tropical Africa, Journal of
980 Geophysical Research: Atmospheres, 2014JD021759, 10.1002/2014JD021759,
981 2014.
982 Tosca, M. G., Randerson, J. T., and Zender, C. S.: Global impact of smoke aerosols
983 from landscape fires on climate and the Hadley circulation, Atmos. Chem. Phys.,
984 13, 5227-5241, 10.5194/acp-13-5227-2013, 2013.
985 van der Werf, G. R., Dempewolf, J., Trigg, S. N., Randerson, J. T., Kasibhatla, P. S.,
986 Giglio, L., Murdiyarso, D., Peters, W., Morton, D. C., Collatz, G. J., Dolman, A.
987 J., and DeFries, R. S.: Climate regulation of fire emissions and deforestation in
988 equatorial Asia, Proceedings of the National Academy of Sciences, 105,
989 20350-20355, 10.1073/pnas.0803375105, 2008.
990 van der Werf, G. R., Randerson, J. T., Giglio, L., Collatz, G. J., Mu, M., Kasibhatla, P.
991 S., Morton, D. C., DeFries, R. S., Jin, Y., and van Leeuwen, T. T.: Global fire
992 emissions and the contribution of deforestation, savanna, forest, agricultural, and
993 peat fires (1997–2009), Atmos. Chem. Phys., 10, 11707-11735,

994 10.5194/acp-10-11707-2010, 2010.
995 Voulgarakis, A., and Field, R. D.: Fire influences on atmospheric composition, air
996 quality and climate, Current Pollution Reports, 1, 70-81,
997 10.1007/s40726-015-0007-z, 2015.
998 Wang, H., Easter, R. C., Rasch, P. J., Wang, M., Liu, X., Ghan, S. J., Qian, Y., Yoon,
999 J. H., Ma, P. L., and Vinoj, V.: Sensitivity of remote aerosol distributions to
1000 representation of cloud–aerosol interactions in a global climate model, Geosci.
1001 Model Dev., 6, 765-782, 10.5194/gmd-6-765-2013, 2013a.
1002 Wang, X., Doherty, S. J., and Huang, J.: Black carbon and other light-absorbing
1003 impurities in snow across Northern China, Journal of Geophysical Research:
1004 Atmospheres, 118, 1471-1492, 10.1029/2012JD018291, 2013b.
1005 Ward, D. S., Kloster, S., Mahowald, N. M., Rogers, B. M., Randerson, J. T., and Hess,
1006 P. G.: The changing radiative forcing of fires: global model estimates for past,
1007 present and future, Atmos. Chem. Phys., 12, 10857-10886,
1008 10.5194/acp-12-10857-2012, 2012.
1009 Westerling, A. L., Hidalgo, H. G., Cayan, D. R., and Swetnam, T. W.: Warming and
1010 earlier spring increase western U.S. forest wildfire activity, Science, 313, 940-943,
1011 10.1126/science.1128834, 2006.
1012 Wiedinmyer, C., Akagi, S. K., Yokelson, R. J., Emmons, L. K., Al-Saadi, J. A.,
1013 Orlando, J. J., and Soja, A. J.: The Fire INventory from NCAR (FINN): a high
1014 resolution global model to estimate the emissions from open burning, Geosci.
1015 Model Dev., 4, 625-641, 10.5194/gmd-4-625-2011, 2011.
1016 Zhang, Y., Fu, R., Yu, H., Qian, Y., Dickinson, R., Silva Dias, M. A. F., da Silva Dias,
1017 P. L., and Fernandes, K.: Impact of biomass burning aerosol on the monsoon
1018 circulation transition over Amazonia, Geophysical Research Letters, 36, L10814,
1019 10.1029/2009GL037180, 2009.
1020 Zhang, Z., Meyer, K., Platnick, S., Oreopoulos, L., Lee, D., and Yu, H.: A novel
1021 method for estimating shortwave direct radiative effect of above-cloud aerosols
1022 using CALIOP and MODIS data, Atmos. Meas. Tech., 7, 1777-1789,
1023 10.5194/amt-7-1777-2014, 2014.

1024 Zhang, Z., Meyer, K., Yu, H., Platnick, S., Colarco, P., Liu, Z., and Oreopoulos, L.:
1025 Shortwave direct radiative effects of above-cloud aerosols over global oceans
1026 derived from 8 years of CALIOP and MODIS observations, Atmos. Chem. Phys.,
1027 16, 2877-2900, 10.5194/acp-16-2877-2016, 2016.
1028

Figure Captions

Figure 1. Seasonal variation of GFED monthly fire (a) organic carbon (OC) and (b) black carbon (BC) emissions (Tg C $month^{-1}$) averaged for the period of year 2003 to 2011 in the global, tropical (25°S to 25°N) and Arctic (60°N to 90°N) regions.

Figure 2. Comparison of modeled seasonal variations of aerosol optical depth (AOD) for the period of 2003-2011 with observations for the same period from the AERONET sites. The upper, middle, and bottom panels represent the sites in southern Africa, South America, and the Arctic, respectively.

Figure 3. Same as Figure 2, but for the comparison of single scattering albedo (SSA) at 550 nm.

Figure 4. Annual mean radiative effect due to aerosol-radiation interactions (REari) (W m^{-2}) averaged over the period of 2003-2011 due to (a) all fire aerosols, (c) fire BC, and (e) fire POM estimated with the method of BBFFBF (left panels), and with the method of Ghan (2013) ((b), (d), and (f) in the right panels). The plus signs in Figure 4(b), (d) and (f) denote the regions where the radiative effect estimated with Ghan [2013] is statistically significant at the 0.05 level.

Figure 5. (a) September-October-November (SON) mean fire aerosol radiative effect due to aerosol-radiation interactions (REari) (W m^{-2}) for the period of 2003-2011 over the Southeast Atlantic Ocean due to all fire aerosols. (b) and (c) are the same as (a), but for the above-cloud aerosol REari for the period of 2007-2011 estimated using Aqua/MODIS and Terra/MODIS products [*Zhang et al.*, 2014], respectively.

Figure 6. Annual mean radiative effect due to aerosol-cloud interactions (REaci) (W m^{-2}) averaged over the period of 2003-2011 due to (a) all fire aerosols, (b) fire BC, and (c) fire POM. The plus signs denote the regions where the radiative effect is statistically significant at the 0.1 level.

Figure 7. Seasonal variation of radiative effect of all fire aerosols due to aerosol-cloud interactions (REaci) (W m^{-2}) for the period of 2003-2011 for (a) December-January-February (DJF), (b) March-April-May (MAM), (c) June-July-August (JJA), and (d) September-October-November (SON). The plus signs denote the regions where the radiative effect is statistically significant at the 0.05 level.

Figure 8. Month-latitude cross sections of zonal mean and monthly (a) vertically-integrated concentrations (mg m^{-2}) of fire BC and (b) fire POM, (c) cloud liquid water path (LWP, in g m^{-2}), (d) low-level cloud cover (CLDLOW, in %), (e) radiative effect due to aerosol-radiation interactions (REari, in W m^{-2}), and (f) radiative effect due to aerosol-cloud interactions (REaci, in W m^{-2}) of all fire aerosols.

Figure 9. Evaluation of CAM5 simulated black carbon (BC) concentration for the period of 2003-2011 (in ng g^{-1}) in the top snow layer against observations in the Arctic [*Doherty et al.*, 2010] and Northern China [*Wang et al.*, 2013b]. The top snow layer ranges in thickness from 1 to 3 cm. Configuration of the two CAM5 simulations (FIRE and NOFIRE) is summarized in Table 1. Panel (a) shows the comparisons at different latitudes. The box and whisker plot in panel (b) shows the minimum and maximum value with the bar, the 25th and 75th percentiles with the box, the 50th percentile (i.e., median) by the bar within the box, and the mean value with the dot.

Figure 10. (a) Annual mean radiative effect due to surface albedo changes (REsac, W m^{-2}) averaged over the period of 2003-2011 of all fire aerosols over land regions, and annual mean surface effect of fire BC-in-snow calculated from SNICAR averaged (b) over all times and (c) only when snow is present. The plus signs in (a) denote the regions where the radiative effect is statistically significant at the 0.1 level.

Figure 11. Annual mean net shortwave flux changes (W m^{-2}) over the period of 2003-2011 (a) at top of the atmosphere, (b) in the atmosphere, (c) at surface, and changes of (d) surface air temperature (TS, K), (e) convective precipitation (mm d^{-1}), and (f) large-scale precipitation (mm d^{-1}) due to all fire aerosols. The plus signs denote the regions where the change is statistically significant at the 0.1 level.

Figure 12. Changes in (a) surface air temperature (K), (b) total precipitation (mm d^{-1}), (c) cloud liquid water path (g m^{-2}), and (d) low-level cloud cover (%) due to all fire aerosols in the boreal summer (JJA) averaged for the period of 2003-2011. The plus signs denote the regions where the change is statistically significant at the 0.1 level.

Table 1. Numerical experiments and associated fire aerosol emissions in each experiment.

Experiment	Ensembles	Fire BC	Fire POM	Fire SO_2
FIRE	10	On	On	On
NOFIRE	10	Off	Off	Off
NOFIREBC	10	Off	On	On
NOFIREPOM	10	On	Off	On
FIRE_BBFFBF	1	On	On	On

Table 2. Global, tropics (25°S to 25°N) and Arctic (60°N to 90°N) annual mean fire aerosol (POM and BC) burdens, fire aerosol AOD, total fire aerosol radiative effect (RE) at TOA, radiative effects due to aerosol-radiation interactions (REari), due to aerosol-cloud interactions (REaci), and due to surface albedo changes (REsac), and changes in cloud liquid water path (LWP), low-level cloud cover, net solar fluxes at surface, shortwave atmospheric absorption, surface air temperature, and precipitation (total, convective, and large-scale) due to all fire aerosols. Standard deviations about the 10-ensemble means are included. The change shown in bold character is statistically significant at the 0.05 level.

	Global	Tropics (25°S to 25°N)	Arctic (60°N to 90°N)
Fire POM burden (mg m^{-2})	**1.25±0.01**	**1.87±0.01**	**1.70±0.08**
Fire BC burden (mg m^{-2})	**0.106±0.001**	**0.17±0.001**	**0.09±0.004**
Fire aerosol optical depth	**0.008±0.001**	**0.012±0.001**	**0.007±0.0004**
Total radiative effect (W m^{-2})	**-0.55±0.07**	**-0.66±0.09**	**-1.35±1.03**
Radiative effect due to ARI (W m^{-2})	**0.16±0.01**	**0.17±0.017**	**0.43±0.028**
Radiative effect due to ACI (W m^{-2})	**-0.70±0.05**	**-0.82±0.09**	**-1.38±0.23**
Radiative effect due to surface albedo changes (over land, W m^{-2})	0.03±0.10	-0.04±0.06	0.09±0.80
Cloud liquid water path (g m^{-2})	**1.62±0.01**	**1.95±0.13**	**2.59±0.25**
Low-level cloud cover (%)	0.012±0.06	**-0.055±0.05**	**0.46±0.45**
Net solar flux at surface (W m^{-2})	**-1.38±0.05**	**-1.91±0.12**	**-2.27±1.04**
Shortwave atmospheric absorption (W m^{-2})	**0.83±0.03**	**1.25±0.04**	**0.92±0.05**
Surface air temperature (K)	**-0.03±0.03**	**-0.024±0.011**	-0.15±0.20
Total precipitation rate (mm day^{-1})	**-0.010±0.002**	**-0.016±0.01**	-0.001±0.02
Convective precipitation rate (mm day^{-1})	**-0.003±0.002**	-0.001±0.009	**-0.005±0.003**
Large-scale precipitation rate (mm day^{-1})	**-0.007±0.002**	**-0.015±0.003**	0.004±0.019

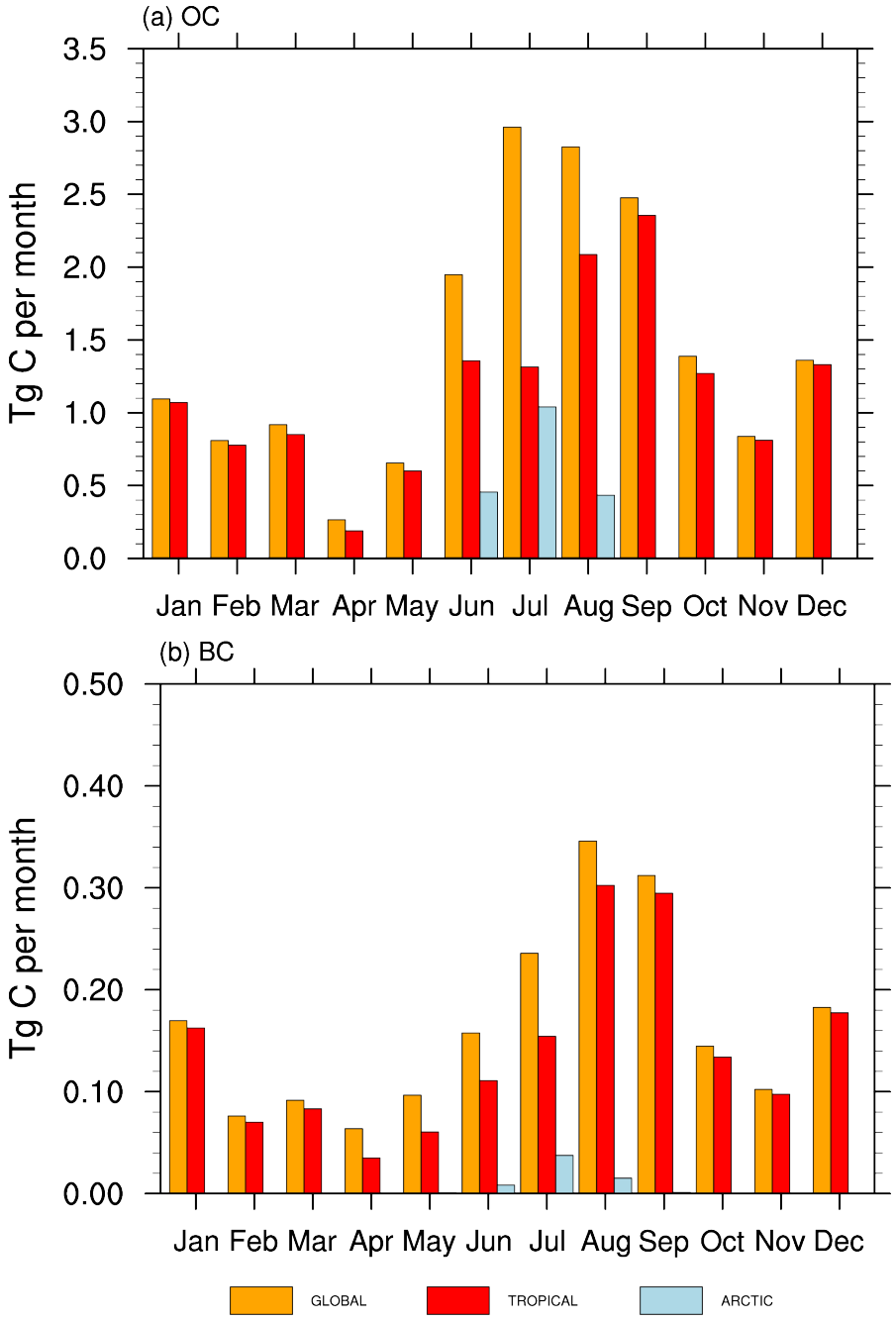

Figure 1. Seasonal variation of GFED monthly fire (a) organic carbon (OC) and (b) black carbon (BC) emissions (Tg C month^{-1}) averaged for the period of year 2003 to 2011 in the global, tropical (25°S to 25°N) and Arctic (60°N to 90°N) regions.

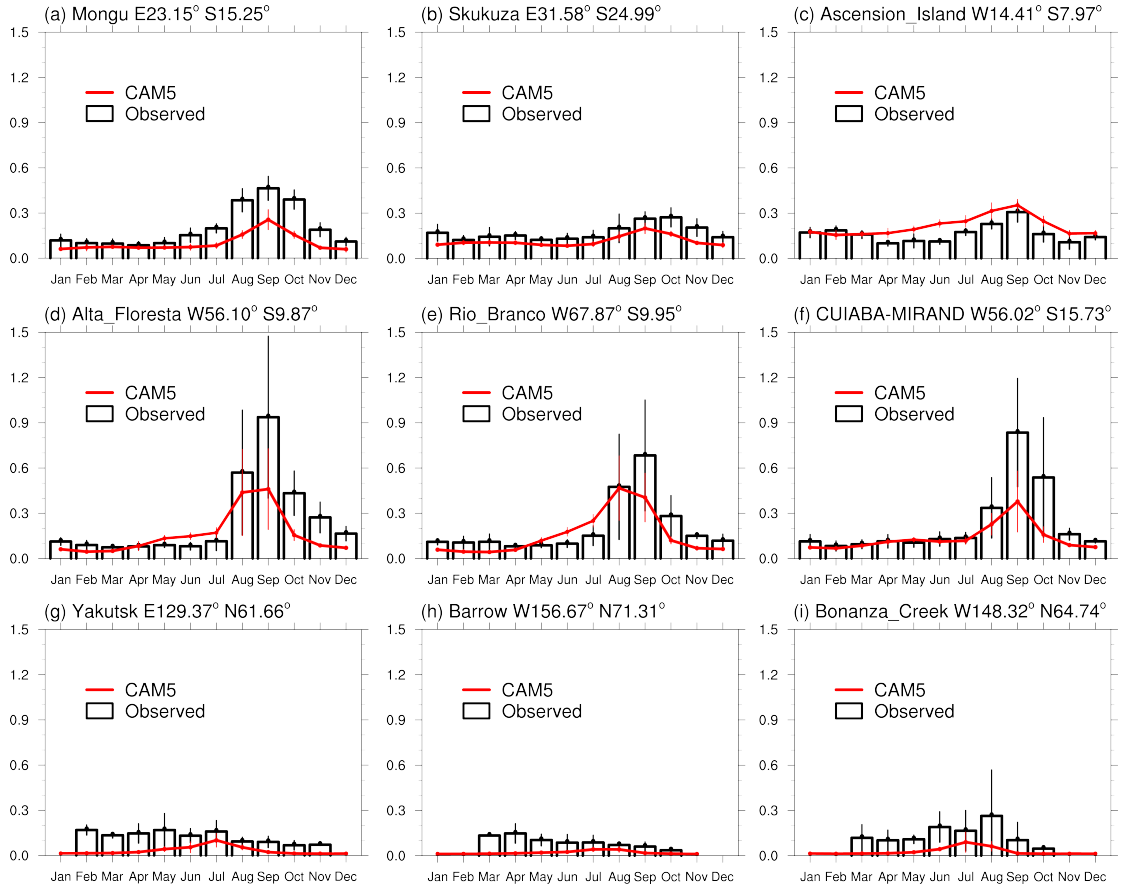

Figure 2. Comparison of modeled seasonal variations of aerosol optical depth (AOD) for the period of 2003-2011 with observations for the same period from the AERONET sites. The upper, middle, and bottom panels represent the sites in southern Africa, South America, and the Arctic, respectively.

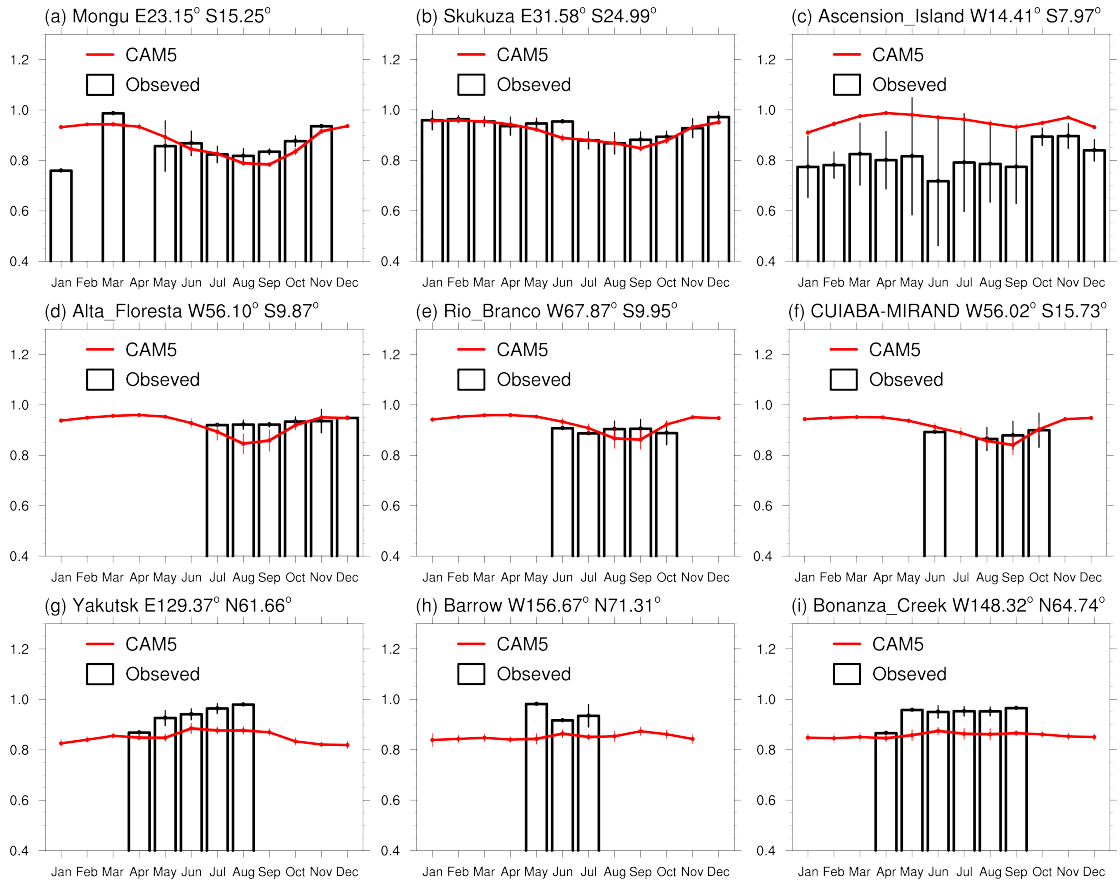

Figure 3. Same as Figure 2, but for the comparison of single scattering albedo (SSA) at 550 nm.

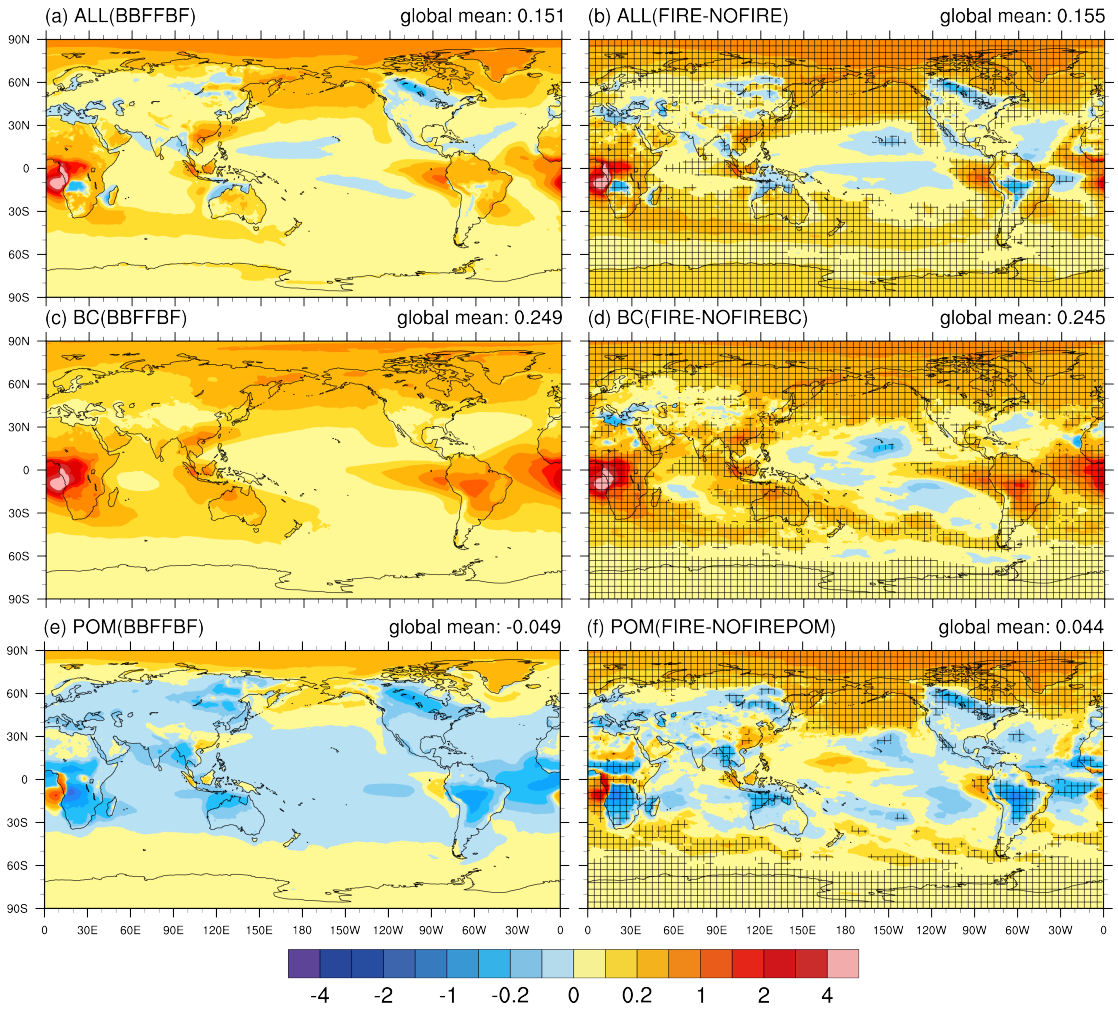

Figure 4. Annual mean radiative effect due to aerosol-radiation interactions (REari) (W m^{-2}) averaged over the period of 2003-2011 due to (a) all fire aerosols, (c) fire BC, and (e) fire POM estimated with the method of BBFFBF (left panels), and with the method of Ghan (2013) ((b), (d), and (f) in the right panels). The plus signs in Figure 4(b), (d) and (f) denote the regions where the radiative effect estimated with Ghan [2013] is statistically significant at the 0.05 level.

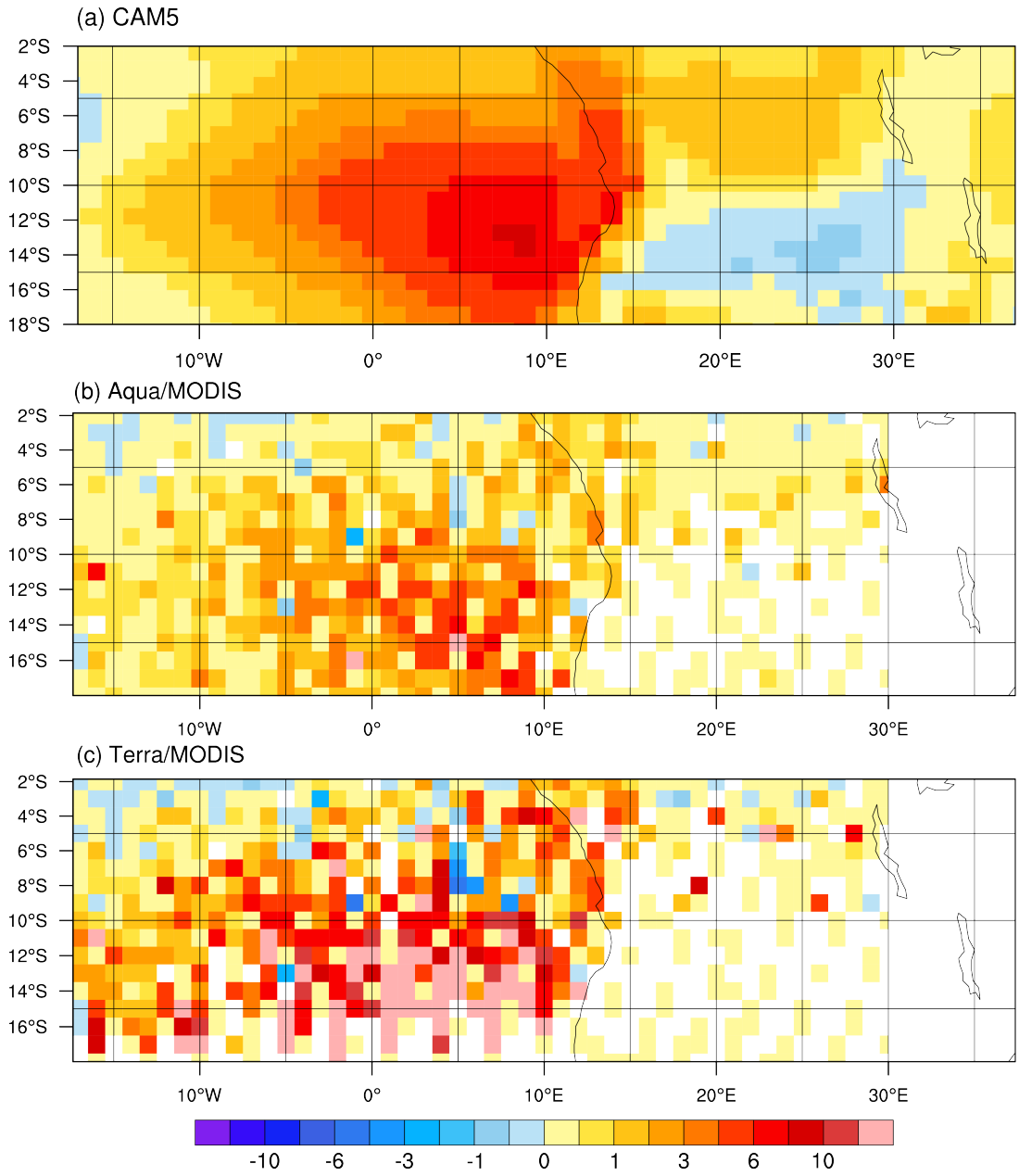

Figure 5. (a) September-October-November (SON) mean fire aerosol radiative effect due to aerosol-radiation interactions (REari) (W m^{-2}) for the period of 2003-2011 over the Southeast Atlantic Ocean due to all fire aerosols. (b) and (c) are the same as (a), but for the above-cloud aerosol REari for the period of 2007-2011 estimated using Aqua/MODIS and Terra/MODIS products [*Zhang et al.*, 2014], respectively.

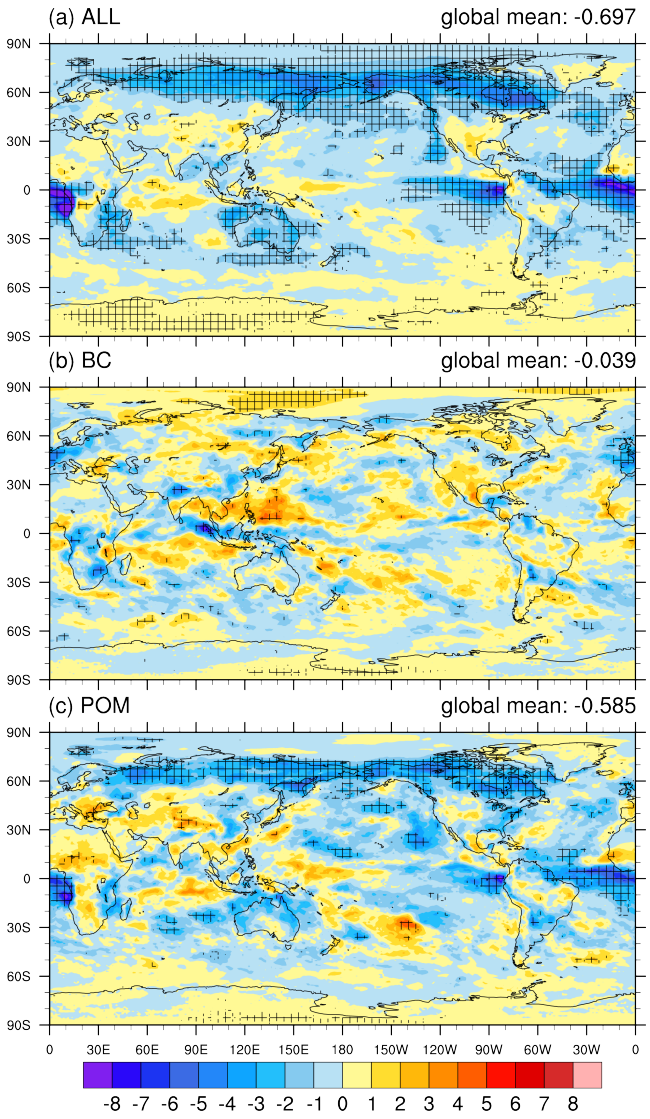

Figure 6. Annual mean radiative effect due to aerosol-cloud interactions (REaci) (W m^{-2}) averaged over the period of 2003-2011 due to (a) all fire aerosols, (b) fire BC, and (c) fire POM. The plus signs denote the regions where the radiative effect is statistically significant at the 0.1 level.

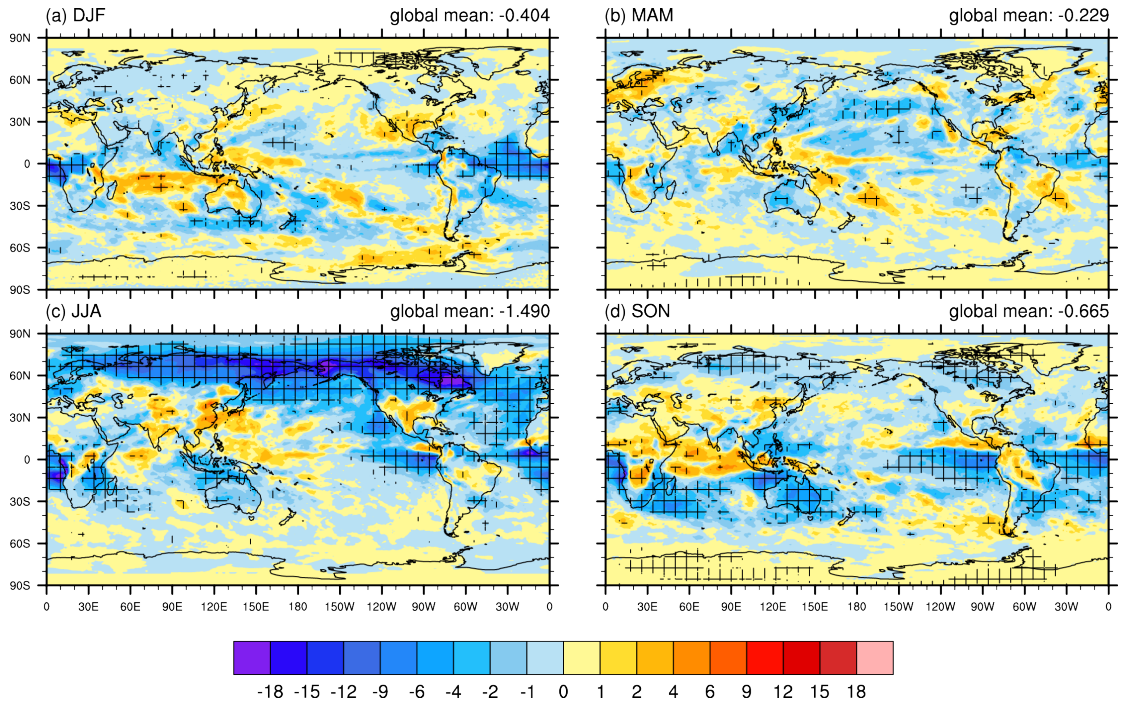

Figure 7. Seasonal variation of radiative effect of all fire aerosols due to aerosol-cloud interactions (REaci) (W m^{-2}) for the period of 2003-2011 for (a) December-January-February (DJF), (b) March-April-May (MAM), (c) June-July-August (JJA), and (d) September-October-November (SON). The plus signs denote the regions where the radiative effect is statistically significant at the 0.05 level.

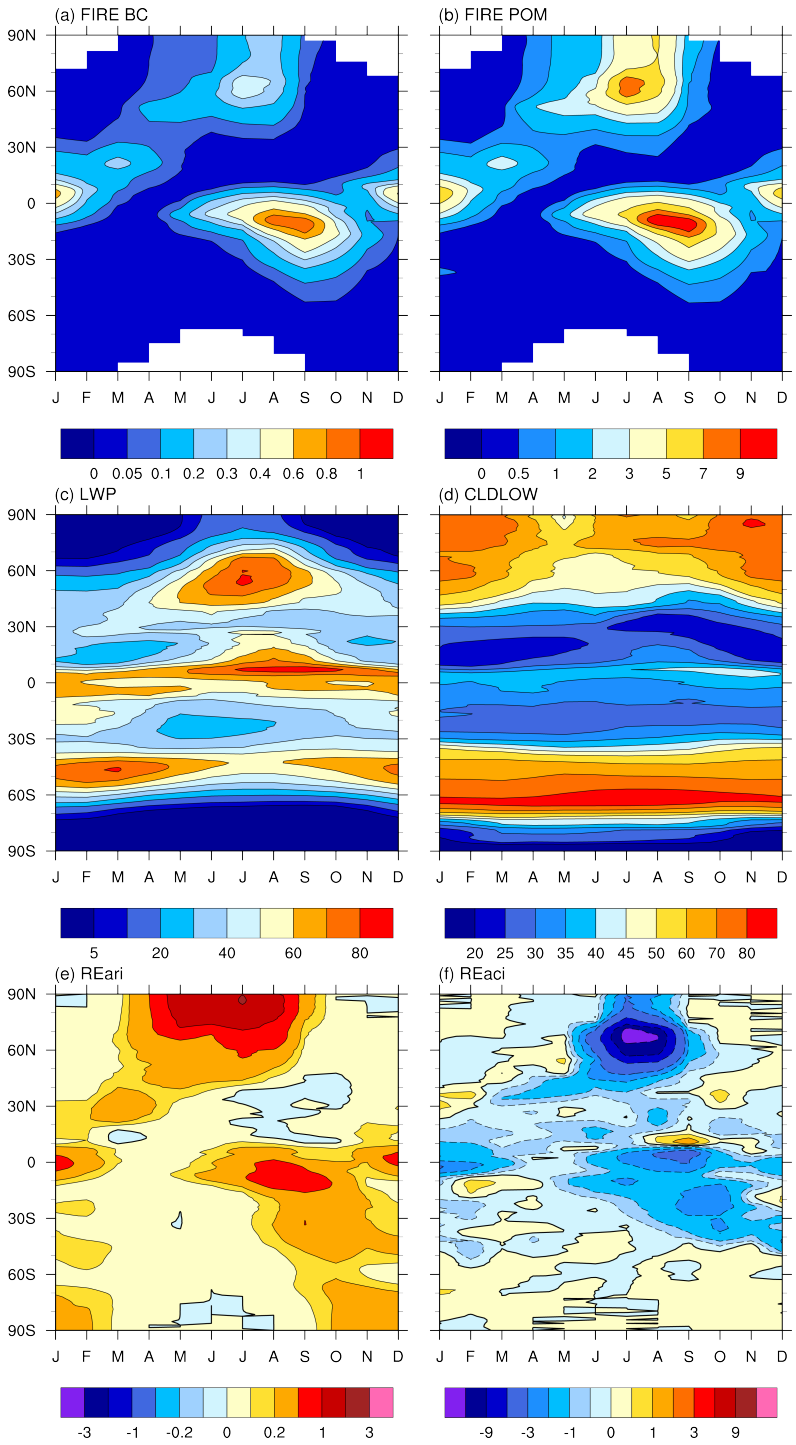

Figure 8. Month-latitude cross sections of zonal mean and monthly (a) vertically-integrated concentrations (mg m^{-2}) of fire BC and (b) fire POM, (c) cloud liquid water path (LWP, in g m^{-2}), (d) low-level cloud cover (CLDLOW, in %), (e) radiative effect due to aerosol-radiation interactions (REari, in W m^{-2}), and (f) radiative effect due to aerosol-cloud interactions (REaci, in W m^{-2}) of all fire aerosols.

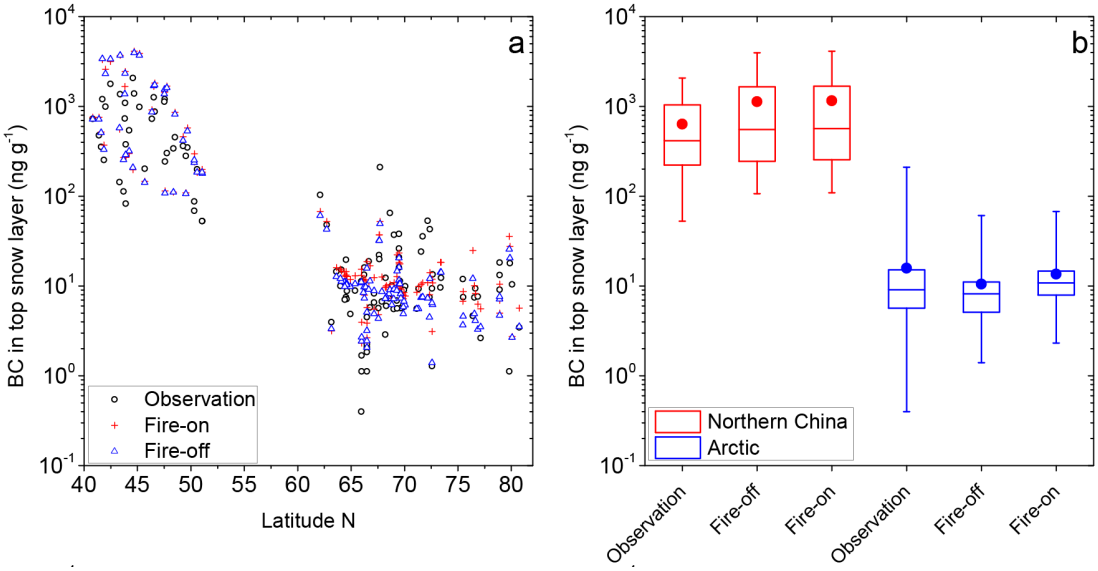

Figure 9. Evaluation of CAM5 simulated black carbon (BC) concentration for the period of 2003-2011 (in ng g^{-1}) in the top snow layer against observations in the Arctic [*Doherty et al.*, 2010] and Northern China [*Wang et al.*, 2013b]. The top snow layer ranges in thickness from 1 to 3 cm. Configuration of the two CAM5 simulations (FIRE and NOFIRE) is summarized in Table 1. Panel (a) shows the comparisons at different latitudes. The box and whisker plot in panel (b) shows the minimum and maximum value with the bar, the 25th and 75th percentiles with the box, the 50th percentile (i.e., median) by the bar within the box, and the mean value with the dot.

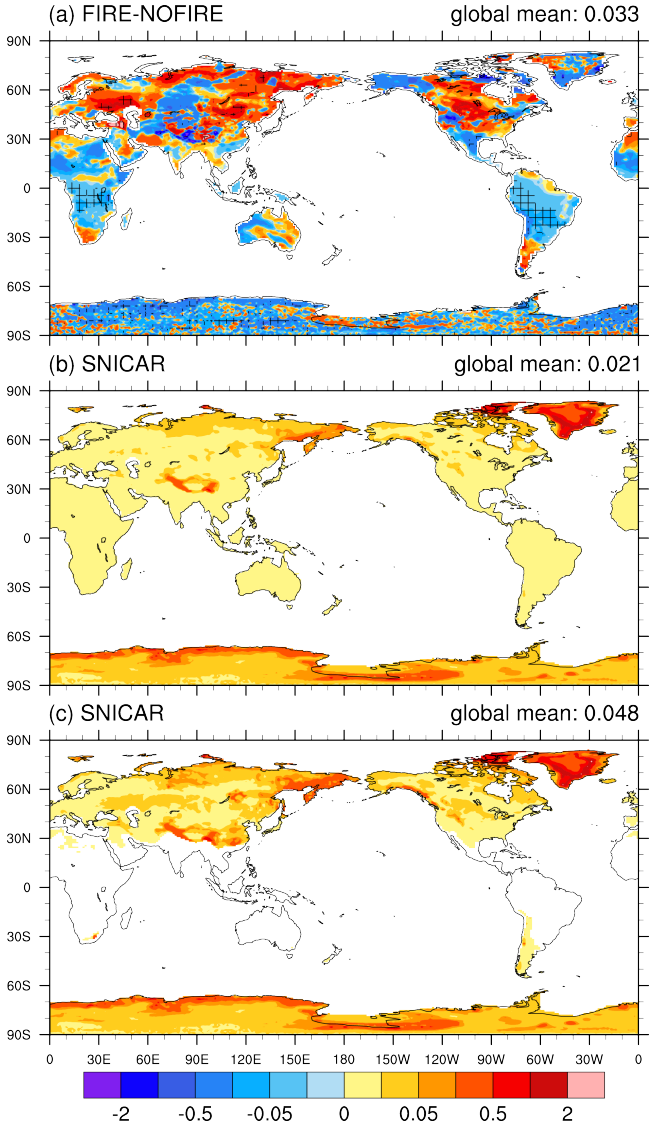

Figure 10. (a) Annual mean radiative effect due to surface albedo changes (REsac, W m^{-2}) averaged over the period of 2003-2011 of all fire aerosols over land regions, and annual mean surface effect of fire BC-in-snow calculated from SNICAR averaged (b) over all times and (c) only when snow is present. The plus signs in (a) denote the regions where the radiative effect is statistically significant at the 0.1 level.

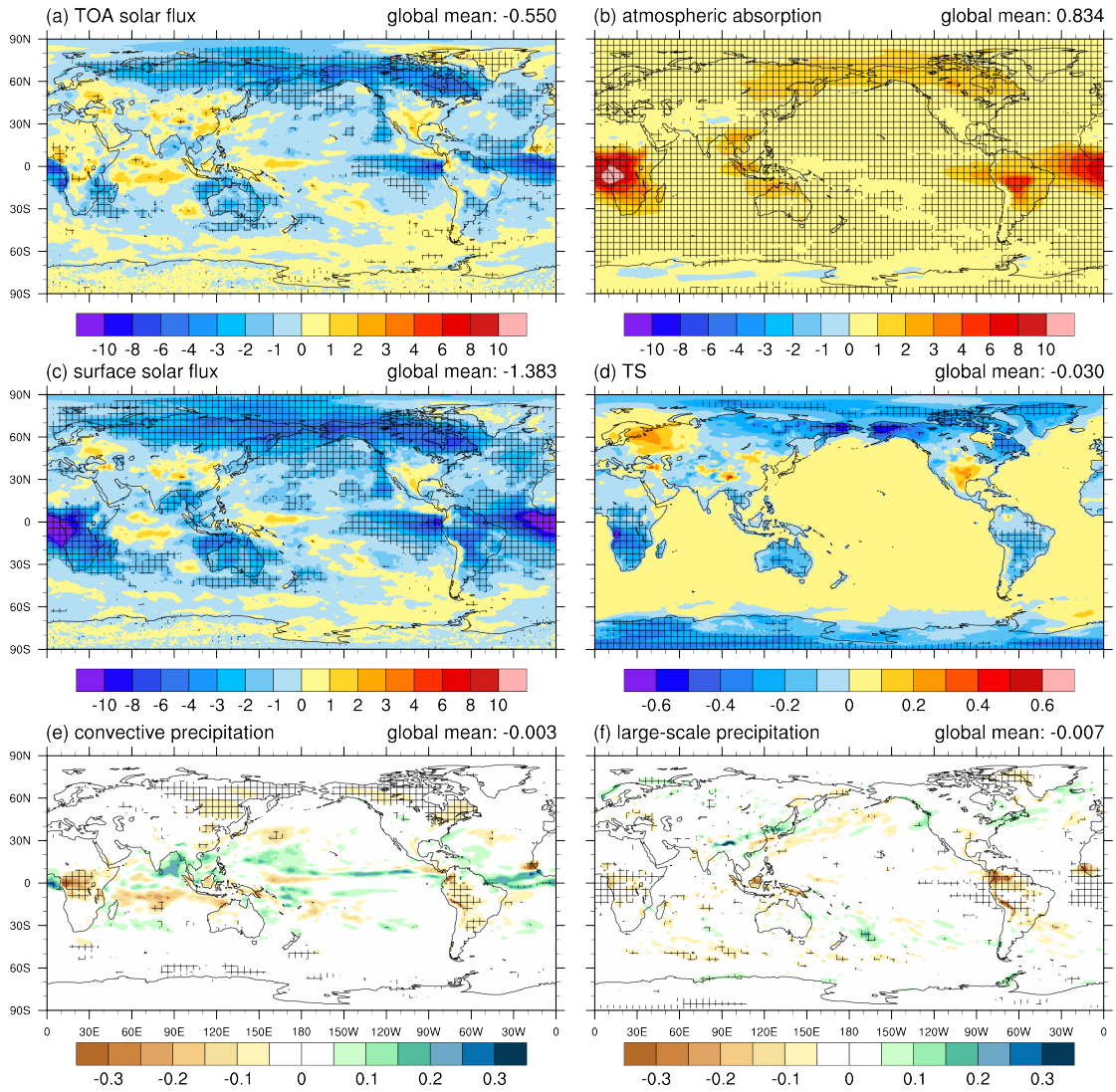

Figure 11. Annual mean net shortwave flux changes (W m^{-2}) over the period of 2003-2011 (a) at top of the atmosphere, (b) in the atmosphere, (c) at surface, and changes of (d) surface air temperature (TS, in K), (e) convective precipitation (mm d^{-1}), and (f) large-scale precipitation (mm d^{-1}) due to all fire aerosols. The plus signs denote the regions where the change is statistically significant at the 0.1 level.

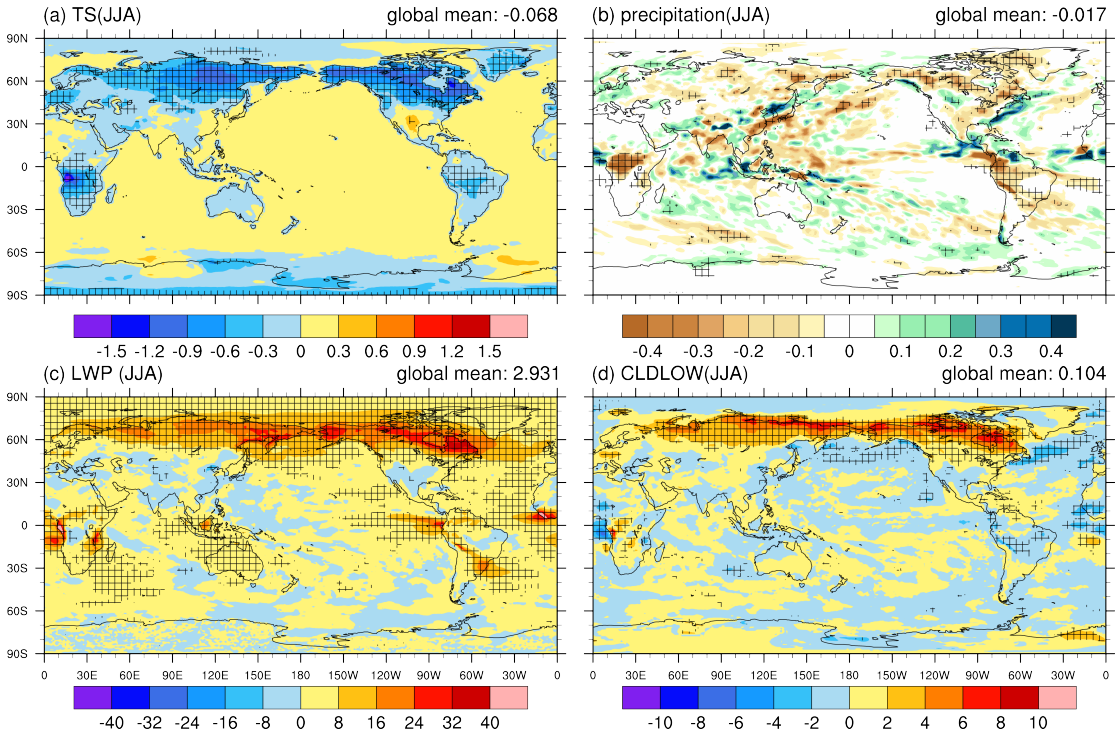

Figure 12. Changes in (a) surface air temperature (TS, in K), (b) total precipitation (mm d^{-1}), (c) cloud liquid water path (LWP, in g m^{-2}), and (d) low-level cloud cover (CLDLOW, in %) due to all fire aerosols in the boreal summer (JJA) averaged for the period of 2003-2011. The plus signs denote the regions where the change is statistically significant at the 0.1 level.